THESIS FOR THE DEGREE OF DOCTOR OF PHILOSOPHY

Quantitative 3D reconstruction of porous polymers using FIB-SEM tomography

Correlating materials structures to properties of coatings for controlled drug release

CECILIA FAGER

CHALMERS

Department of Physics
CHALMERS UNIVERSITY OF TECHNOLOGY
Gothenburg, Sweden 2020

Quantitative 3D reconstruction of porous polymers using FIB-SEM tomography
Correlating materials structures to properties of coatings for controlled drug release
Cecilia Fager

ISBN 978-91-7905-301-7
Doktorsavhandlingar vid Chalmers Tekniska Högskola, Ny serie nr 4768
ISSN 0346-718X

Department of Physics
Chalmers University of Technology
SE – 412 96 Gothenburg
Sweden
Telephone + 46 (0)31-7723334

Cover illustration:
The figure on the cover shows (middle) a scanning electron microscopy secondary electron image of a pellet and the internal porous structure. The outer image circle shows, starting from the left and going clockwise, FIB-SEM data of a porous polymer film; segmented FIB-SEM data; through paths with a limiting layer highlighted in yellow; tortuosity, mass transport simulations showing flux lines for the diffusion transport; and an illustration of the manufacturing of pellets using a fluidised bed.

Printed by Chalmers Reproservice
Gothenburg, Sweden 2020

Quantitative 3D reconstruction of structures in porous polymers using FIB-SEM tomography
Correlating materials structures to properties of coatings for controlled drug release

Cecilia Fager

Department of Physics
Chalmers University of Technology

Abstract

Porous networks are found in a wide range of different advanced and technologically important materials and influence the materials properties. The networks are active components in for example batteries, food and pharmaceuticals. The interconnectivity of a network strongly influences the transport properties. One example is polymer film coatings for controlled drug release where the porous network acts as a transport path for drugs. The correlation between the detailed structure of the network and the transport properties illustrates the importance of quantifying the interconnectivity in 3D. One approach to image material in 3D is sequential imaging (tomography). Examples of tomography techniques are confocal laser scanning microscopy, x-ray and neutron tomography where the spatial resolution is limited to the micrometre length scale. Transmission electron microscopy tomography and focused ion beam (FIB) combined scanning electron microscope (SEM) tomography are examples of techniques with higher spatial resolution ranging from micrometre to sub-nanometre.

In this work the focus is on the understanding of the correlation between the structure and materials properties of phase-separated polymer film coatings used for controlled drug release. We acquired high spatial 3D resolution data on microporous ethyl cellulose and hydroxypropyl cellulose film coatings using FIB-SEM tomography. The tomography was performed after the water soluble hydroxypropyl cellulose phase had been removed leaving a porous network providing a transport path for the drug. We optimised the FIB-SEM parameters and established a generic protocol for porous and poorly conducting materials in order to overcome challenges such as redeposition, curtaining, shadowing effects, charging and sub-surface information due to the pores. In addition, a new self-learning segmentation algorithm was introduced to enable an automatic separation between pores and matrix. The quantification of the porous network was carried out by determining the pore size distribution, tortuosity and interconnectivity. As a final step, diffusion simulations were performed on the FIB-SEM data and correlated with experimentally measured permeability.

Keywords: focused ion beam, scanning electron microscopy, tomography, 3D, soft material, insulating material, connectivity, polymer film, controlled drug release

Following papers are included in this thesis:

Paper I **Optimisation of FIB-SEM tomography and reconstruction for soft, porous and poorly conducting materials**

C. Fager, M. Röding, A. Olsson, C. von Corswant, N. Lorén, A. Särkkä and E. Olsson. *Accepted for publication in Microscopy and Microanalysis. (2020).*

Paper II **Three-dimensional reconstruction of porous polymer films from FIB-SEM tomography data using random forests**

M. Röding, C. Fager, A. Olsson, C. von Corswant, A. Särkkä, E. Olsson and N. Lorén. *Manuscript submitted.*

Paper III **3D high spatial resolution visualisation and quantification of interconnectivity in polymer coatings**

C. Fager, S. E. Barman, M. Röding, A. Olsson, C. von Corswant, N. Lorén, H. Rotzén, D. Bolin and E. Olsson. *Under review in International Journal of Pharmaceutics.*

Paper IV **New characterization measures of pore shape and connectivity applied to polymer film coatings used for controlled drug release**

S. Barman, C. Fager, M. Röding, A. Olsson, C. von Corswant, N. Lorén, D. Bolin, H. Rotzén and E. Olsson. *Manuscript intended for Soft Matter.*

Paper V **Correlating 3D porous structure with mass transport properties in polymer films using FIB-SEM tomography**

C. Fager, J. Hjärtstam, T. Gebäck, M. Röding, C. von Corswant, A. Olsson, N. Lorén, A. Särkkä and E. Olsson. *Manuscript intended for The Journal of Physical Chemistry B.*

Paper VI **Revealing the porous structure of pellet film coatings used for controlled drug release dosage forms**

C. Fager, C. von Corswant, A. Viridén, , M-O. Johansson, A. Olsson, M. Röding, N. Lorén, A. Särkkä and E. Olsson. *Manuscript intended for International Journal of Pharmaceutics.*

Paper VII **Revealing regions with different transport characteristics in coatings for controlled drug release by 3D visualisation**

C. Fager, C. von Corswant, A. Olsson, M. Röding, T. Nilsson Pingel, N. Lorén, A. Särkkä, E. Olsson. *Manuscript.*

My contributions to the appended papers:

Paper I I did all the microscopy work and optimised the imaging procedure, led the evaluation in discussion with my co-authors. I wrote the first draft of the manuscript.

Paper II I did all the microscopy work, manually segmented data that was used to train the segmentation-algorithm, took part in discussions and wrote part of the manuscript.

Paper III I did all the microscopy work, led the evaluation in discussion with my co-authors and I wrote the first draft of the manuscript.

Paper IV I did all the microscopy work, took part in discussions with my co-authors and wrote parts of the manuscript.

Paper V I did all the microscopy work, I performed release measurements, led the evaluation in discussion with my co-authors and I wrote the first draft of the manuscript.

Paper VI I did all the microscopy work, took part in the manufacturing of the material, lead the evaluation in discussion with my co-authors and wrote the first draft of the manuscript.

Paper VII I did all the microscopy work, took part in image post processing, led the evaluation in discussion with my co-authors and wrote the first draft of the manuscript.

In addition to the above papers, I have contributed to the following work, which is not included in this thesis:

Book chapter **Soft materials and coatings for controlled drug release**
Nanotechnologies in Preventive and Regenerative Medicine an Emerging Big Picture. V. Uskokovic and D. P. Uskokovic
C. Fager and E. Olsson. *Netherlands: Elsevier. 2018, 244-259.*

Paper **Fabrication and characterization of plasmonic nanopores with cavities in the solid support**
B. Malekian, K. Xiong, G. Emilsson, J. Andersson, C. Fager, E. Olsson, E.M. Larsson-Langhammer and A.B. Dahlin. *Sensors 2017*, **17**(6), 1-11.

Cecilia Fager

Gothenburg,13th of May 2020

Preface

The research presented in this thesis was carried out in the division of Eva Olsson Group in the Department of Physics, Chalmers University of Technology, Gothenburg, Sweden during the period October 2015 – June 2020, under the supervision of Prof. Eva Olsson and assistant supervisors Dr. Christian von Corswant, Adj. Prof. Niklas Lorén and Prof. Aila Särkkä. This work was funded by the Swedish Foundation of Strategic Research.

List of Abbreviations

BSE	Backscattered electron
EC	Ethyl cellulose
FIB-SEM	Focused ion beam scanning electron microscope
HPC	Hydroxypropyl cellulose
GIS	Gas injection system
D_{eff}	Effective diffusion coefficient
SE	Secondary electron
2D	two-dimensional
3D	three-dimensional
% wt	percent weight
w/w	weight/weight

Acknowledgments

My PhD Journey has been the most fun as well as challenging I ever done in my entire life and I have so many humans I want to thank for making this journey a true pleasure that I will remember for the rest of my life. I would like to start with expressing my gratitude to **Prof. Eva Olsson**. You have been supporting me from day one of my PhD journey. Thank you for giving me this amazing opportunity to do what I love to do which is scientific work utilising electron microscopy at its forefront. I truly appreciate your honesty and for helping me open up my eyes for the broader perspective. Thank you for being you and for these years that have passed filled with exciting scientific discussions, laughter and a lot of hard work.

I would like to thank my co-supervisors, **Adj. Prof. Niklas Lorén** (RISE), **Prof. Aila Särkkä** (Dept. of Mathematical Sciences) and **Dr. Christian von Corswant** (AstraZeneca). Adj. Prof. Niklas Lorén, I really enjoyed our discussions and I am very thankful for the positive energy you given me throughout the years. Prof. Aila Särkkä, you are one of the most humble humans I have met. You always share your supporting smile and expertise. Dr. Christian von Corswant, thank you so much for sharing your expertise with me and for always being there to support me. I truly enjoyed writing papers together with you as well as laughing together. You once asked me when I showed you my beloved FIB-SEM "Isn't it just to press one button on the microscope to get the image?" that phrase will forever make me laugh. I would also like to express my gratitude to my examiner, **Prof. Patrik Johansson**, for great reflections and comments along my PhD Journey.

I would like to acknowledge the Swedish Foundation for Strategic Research (SSF) for funding my fun and exciting PhD project. This project has brought me new scientific skills as an electron microscopist in materials sciences which I will carry with me into the future. In addition, this interdisciplinary project tied bands between scientists from different research fields. Dear **Dr. Sandra Barman**, my PhD colleague from Dept. of Mathematical Sciences and my dear friend, interdisciplinary research was quite challenging in the beginning before we started to understand each other's scientifically language. This challenge did later on turn into our strength based on the interdisciplinary research papers we have created together. **Dr. Magnus Röding** (RISE), the passion I share for electron microscopy, you share for computations and data processing. I want you to know that I have really enjoyed working together with you. I want to thank **Dr. Tobias Gebäck** for a really great collaboration and for always taking his time for discussions. I also want to thank **Dr. Mats Josefsson**, **Prof. Mats Rudemo**, **Prof. Holger Rotzén, Dr. Henrike Häbel** and **Dr. David Bolin** for interesting discussions during our SSF meetings. I want to express my gratitude to **Prof. Niels de Jonge**, for truly exciting and very fruitful discussions about electron microscopy during the SSF advisory board meeting as well as conferences.

Furthermore, I would like to acknowledge AstraZeneca and especially thank **Dr. Anna Olsson**, **Dr. Johan Hjärtstam, Dr. Anna Viridén and Mats-O Johansson** for their expertise and valuable input to this work. Dr. Anna Olsson, the time you have spent on reading and giving comments on all the papers is priceless, thank you so much for this great collaboration. Thank you Dr. Johan Hjärtstam for a great and informative time in the lab as well as fun times writing the paper with you. Thank you Mats-O Johansson for bringing me into the lab and for teaching me about production of pellets in fluidised bed, I will always remember that! I want to thank

Dr. Anna Viridén for contributing with scientific expertise as well as exciting results which turned out in a really exciting paper.
The SOFT Microscopy meetings have brought me interesting ideas as well as great discussions from the participants. I would like to thank **Dr. Mats Stading** and **Annika Altskär** (RISE) as well as **Dr. Eskil Andreasson** (Tetra Pak Packaging Solutions AB) for valuable discussions. I would like to especially thank Annika Altskär for the cryo-electron microscopy discussions as well as all the laughers we shared throughout the years.
My colleagues within Eva Olsson Group, you are the definition of perfect colleagues to me. We always share laughter and supporting each other. I want to give a thanks to **Dr. Andrew Yankovich** for always asking questions that makes me think twice, **Dr. Torben Nilsson Pingel** for being a very supportive and kind office mate, **Dr. Lunjie Zeng** for always supporting me, **Prof. Wolfgang Jaeger** for valuable insight into research, **Dr. Shun Kondo for** bringing scientific expertise and joy to the group. **Pierre Carmona, Gustav Persson, Xin Wen, Fredrik Söderberg and Jonatan Holmér,** thank you all for sharing your opinions and I wish you all the best of luck with your PhD journeys. I would also like to express my gratitude to the members of the advisory board of Eva Olsson Group **Prof. Robert Sinclair** (Stanford University), **Prof. Rafal Dunin-Borkowski** (Ernst Ruska-Centre, Julich), **Prof. David J. Smith** and **Prof. Martha McCartney** (Arizona State University) for giving me valuable advices and insights during the advisory board meetings.
I would also like to give a huge thanks to my colleagues in the group of Materials Microstructure for filling the lunch breaks with laughter where I always learn something new.
CMAL (Chalmers Materials Analysis Laboratory), thank you all for sharing your amazing skills and always being there to help whenever challenges appear by the electron microscopes or elsewhere. Especially a big thanks to **Dr. Stefan Gustafsson** for supporting me at the Gaia FIB-SEM and for becoming a great friend of mine. You made my tough times easier with your presence. I will also direct a huge thanks to **Ola Löfgren** who have solved all my computer challenges throughout the years.
I would like to say thanks to **Daniel Dinesen Jensen** (NordicNano Solutions AB) for amazing service support with the Tescan Gaia FIB-SEM whenever it was required. It has been a true joy to me to learn about microscopes by watching over your shoulder. In addition, I would like to express my thanks to **Dr. Hana Tesarova** (Tescan Orsay Holdings). Thank you Dr. Hana Tesarova for teaching me all the basics there is to know in order to operate the Gaia FIB-SEM. This made my FIB-SEM foundation from where I further developed my skills as an electron microscopist.
Finally, no words can ever describe the love and support my lovely family have given me throughout this journey. I would like to send my love to my dad **(Anders Fager)**, mom (**Ingalill Fager**) and brother (**Patrik Fager**) who have always been there to catch me whenever I fall (yes, we all do that sometimes) as well as sharing my happiness when those indescribable electron microscopy moments appears after years of well invested time. My last thanks goes the human, the love of my life (**Sebastian Pimenoff**), who made me realise that there is a life outside work that is truly amazing to live.

CONTENTS

Chapter 1
Introduction

1.1 Background

Porous networks are present in a wide range of different advanced and technologically important materials and influence the materials properties. The networks are active microstructural components in, for example, batteries, food and pharmaceuticals. The interconnectivity of the network strongly influences the transport properties. It is of great importance to understand the correlation between the microstructure of the porous network and the properties of the materials in order to optimise them for different applications. For example, porous networks in polymer film coatings can be used to control drug release (Siepmann, *et al*., 2007). Another example where the porous network influences the transport properties is in biological materials such as scaffolds used for bone ingrowth (Jones, *et al*., 2009; Subramaniam, (2005). Another example is porous networks in solar cells, fuel cells and batteries that play very important roles for the electric and ionic conductivity (Stenzel, *et al*., 2016; Holzer, *et al*., 2013).

One way to increase the understanding of materials properties is to visualise their structures in three-dimensions (3D). There exist several well-established imaging techniques and the choice of which to utilise depends on various factors such as what type of material and desired resolution of the structural information. Electron microscopes provide the possibility to study structures with high spatial resolution. The conventional scanning electron microscope (SEM) is imaging materials by rastering an electron beam over the material surface. An SEM has one main criteria that needs to be fulfilled which is to operate under vacuum, hence, liquid containing materials are not suitable to be imaged in an SEM. However, further developments of the SEM instruments have resulted in that gas can be allowed into the chamber. This instrument is known as a low vacuum – scanning electron microscope (LV-SEM). The LV-SEM can be used to image soft materials such as polymers (Stokes, *et al*., 2008; Jansson, *et al*., 2013). Moreover, when the aim is to reveal and image the internal structure of a material, a focused ion beam (FIB) instrument combined with a scanning electron microscope (SEM) can be utilised. The combined instrument uses the ions to remove material with high spatial

precision, below 10 nm, and create planar cross sections. The electrons are utilised to image the revealed cross section surface with high spatial resolution down to 1 nm.

The FIB with a liquid-metal-ion-source has been around since 1979 and was initially used as a tool for sample preparation (Seliger, *et al*., 1979). Further development of the instrument resulted in a variety of applications and one of them was FIB tomography (Kirk, *et al*. 1987). The tomography procedure involves to perform serial sectioning of thin slices and to image each cross-section surface. In a FIB, both the milling and the imaging are performed using the ion beam. It was quickly noted that the ion beam damaged the surface even during imaging. The next generation of instruments introduced the combination of FIB and SEM. This provided the opportunity to image using the electron beam without damaging the surface (Inkson, *et al*., 2001). The FIB-SEM could now also be used for high spatial resolution 3D data acquisition using the ion beam for high precision serial sectioning and the electron beam for imaging with high spatial resolution (Goldstein, *et al*., 2003; Holzer, *et al*., 2004; Heymann, *et al*., 2006; Hayles, *et al*., 2007; Michael, 2011; Cantoni & Holzer, 2014). The method is nowadays routinely applied to highly conducting materials such as metals and ceramics (Bassim, *et al*., 2014; Cantoni, *et al*., 2014; Holzer, *et al*., 2004). However, for soft materials such as biological samples, 3D FIB-SEM data acquisition remains challenging (Bassim, *et al*., 2011; Narayan, *et al*., (2015). The problems are charging and damage induced by the ion and electron beams as well as the low contrast in images of soft materials (Wolff, *et al*., 2018; Deng, *et al*., 2015). From previous findings, several examples of extensive sample preparations and cryogenic approaches have resulted in successful imaging of poorly conductive materials (Brostow, *et al*., 2007; Kim, *et al*., 2011; Dubochet, *et al*., 1988; Villinger, *et al*., 2012; Kizilyaprak, *et al*., 2019; Parmenter, *et al*., 2016).

1.2 Scope of the thesis

The focus of this work was to understand the correlation between structure and transport properties of soft, porous and poorly conducting materials. Therefore, a special effort was made to visualise the detailed structures in 3D with high spatial resolution. In addition, quantification of the porous network was of great interest in order to explore and determine the structural features giving rise to the transport properties of the porous material. The experimental methods and the quantification to correlate the structure to properties are generic interest for this type of porous materials. Here, polymer film coatings intended for controlled drug release was studied. They consisted of phase-separated polymer blends of ethyl cellulose and hydroxypropyl

cellulose where the latter phase was water soluble. After exposure to water the hydroxypropyl cellulose phase dissolved leaving a porous network that provided a path for drug release. The 3D visualisation was performed using FIB-SEM.

1.3 Outline of the thesis

This thesis is structured in the following way: Chapter 2 describes the basic concepts of porous polymer film coatings used for controlled drug release. In Chapter 3, the investigated porous polymer film coatings are introduced. The characterisation methods used in this thesis are presented in Chapter 4. Chapter 5 contains the main results obtained in this thesis, the full details are found in the appended papers. Finally, conclusions are presented in Chapter 6 and an outlook in Chapter 7.

Chapter 2

Controlled drug release using polymer film coatings

2.1 Soft materials for controlled drug release

The overall goal of a pharmaceutical product is to obtain an optimum therapeutic as well as tailored treatment for its purpose (Klein, 2002). In order to achieve this overall goal, a combination of an effective active pharmaceutical ingredient (API) and a tailored controlled release rate is required (Hutton, *et al*., 1992). In addition, a minimisation of the total amount of drug that is needed and an elimination of plausible side effects is desired (Edsbäcker, *et al*., 2003; Anderson, *et al*., 1999). Pellets, which is a multiple unit dosage form, are frequently used for oral controlled drug delivery (Muschert, *et al*., 2009). Pellets consist of a core that has been coated with API as well as a phase-separated polymer film coating used for controlling the drug release (Ozturk, *et al*., 1990). Controlled drug release coatings have been around for more than 50 years and their performance has increased significantly since their beginning partly due to a more controlled chemistry during the fabrication (Rhodes, *et al*., 1998). There exist different important aspects that need to be considered in order to obtain the specific drug release behaviour that is envisioned. One aspect that is of great importance to be considered is the gastrointestinal tract (GI). It is where the drug release will occur and be further directed to the targeted location (Gruber, *et al*., 1987). Different pH-values exists throughout the GI tract (Rawlings, *et al*., 1985). It does also need to be pointed out that the pH-values within the GI tract also vary depending on feed or starving condition. The different pH-values need to be taken into account when selecting a soft material to be used as controlled release coating. This is due to that different materials have different solubilities at different pH-values.

The source of the polymers can be either natural or synthetic. A common constituent of these types of coatings is cellulose derivative (Langer, *et al*., 1983). One major advantage with cellulose is that it is non-toxic and harmless. Cellulose derivatives are modified cellulose, and they possess a great variability since they can be modified by adding substitution groups to the backbone. Therefore, a two-component coating could consist of one hydrophilic cellulose and one hydrophobic cellulose, depending on the added substitution groups.

2.2 Polymer phase separation

The procedure of how to coat a drug core with a phase-separated polymer film, intended for controlled drug release, is well-established (Siepmann, *et al*., 2008). The phase separation kinetics during the manufacturing process controls the microstructure of the films. The microstructure provides the transport path for the drug. One way to coat the drug core with the phase-separated polymer film is to spray a solution onto the drug core. The solution consists of two immiscible polymers dissolved in a solvent. When the solvent evaporates, a phase separation between the two immiscible polymers occurs (Jones, *et al*., 1999). Even though there are several ways of going from a one-phase solution (two immiscible polymers are dissolved with a solvent) to a two-phased solution (two immiscible polymers have been phase separated), the following three examples will be used to explain phase separation. One way to induce phase separation is to change the temperature, see Figure 1a). When the temperature is lowered, the one-phase solution turns into a two-phase solution. Another way to turn a one-phase solution into a two-phased solution is to evaporate the solvent, see Figure 1b). A third way could be to increase the degree of polymerisation, see in Figure 1c).

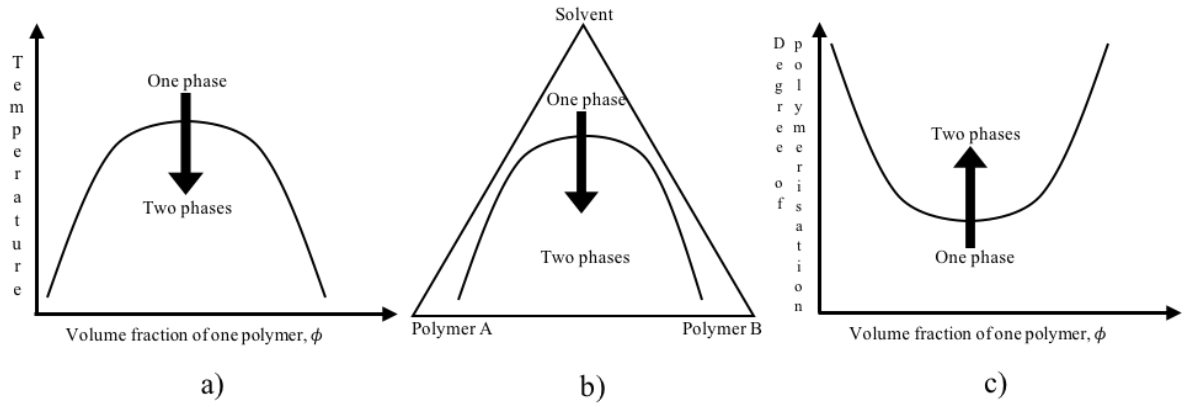

Figure 1. Illustration of three different factors that can cause phase separation where a) shows that cooling of a solution of two immiscible polymers with a solvent results in a phase separation. b) shows that evaporation of the solvent can cause phase separation and c) shows that a higher degree of polymerisation causes phase separation (adapted from Jones, *et al*., 1999).

2.3 EC/HPC phase-separated polymer film coatings

In literature, it has been shown that ethyl cellulose (EC) provides a coherent film and is therefore often selected to be added as the majority polymer in polymer solutions utilised for coatings for controlled drug release (Sakellariou, *et al*., 1995; Lecomte, *et al*., 2003). Hence, the EC is defined as the matrix material of the coatings. Hydroxypropyl cellulose (HPC) is water soluble and provides a porous structure within the coatings upon contact with water, hence defined as the pore former (Siepmann, *et al*., 2007). The solvent utilised to dissolve the two immiscible polymers can, for example, be ethanol. The polymer phase separation is initialised by the ethanol evaporation. As a consequence of the evaporation, phase separation occurs and EC-rich and HPC-rich phases are formed (Norton & Frith, 2001). Depending on the composition regime, discontinuous or bicontinuous structures are formed. The phase separation mechanism resulting in bicontinuous structures is called spinodal decomposition (Jones, *et al*., 1999). The film structure is kinetically trapped by a high film viscosity which is reached at a certain ethanol concentration during the evaporation (Marucci, *et al*., 2013). By immersing the phase-separated polymer films into water, the HPC leaches out. This creates a porous structure within the EC matrix (Siepmann, *et al*., 2007). The porous structure acts as the transport path for the drug.

It has been shown that the release properties of the EC/HPC films can be varied by varying different factors such as process parameters during the manufacturing or the molecular weights for the polymers (Marucci, *et al*, 2013; Andersson, *et al*, 2013). It was found that an increased molecular weight resulted in a decreasing film permeability (Andersson, *et al*., 2018, Andersson, *et al*., 2016). In addition, varying the polymer blend ratio of the two polymers showed that there is a threshold existing around 22 percentage of added HPC where bicontinuous structures are formed. An onset of the film percolation was found at 22 percentage of added HPC (Marucci, *et al*., 2009).

The release mechanism of a model compound consisting of free standing EC/HPC phase-separated polymer films have been studied using a release cell equipped with a manometer (Marucci, *et al*., 2009). It was found that the release rate increased with increased amount of added HPC. In addition, the release mechanism changed from osmotic pumping to diffusion as the amount of HPC was increased.

Furthermore, a new mechanistic model of drug release by osmotic pumping and diffusion from pellets described the main processes in detail (Marucci, *et al*., 2010). In this study, the pellets consisted of SiO_2 cores surrounded by the drug metoprolol succinate coated with a semipermeable film of EC:HPC being 80:20, i.e. close to the percolation onset. The

semipermeable film initially had no pores and was permeable to water but not the drug. The processes occurring during the drug release were as follow: An inlet of the water into the pellet occurred due to the difference in osmotic pressure across the coating which led to dissolving the drug. The inlet of the water caused swelling of the pellet due to the mass accumulation which resulted in a build-up of hydrostatic pressure inside the pellet. Finally, an outflow occurred of the dissolved drug through water-filled paths. These paths may have been pores produced in the coating by the leaching of water-soluble polymer HPC. Another explanation for these paths in the coating could have been micro-cracks created in the coating caused by the build-up of hydrostatic pressure inside the pellet.

Chapter 3
Materials

In this work, two types of soft, porous and poorly conductive samples have been investigated. The samples are phase-separated polymer films consisting of ethyl cellulose (EC) and hydroxypropyl cellulose (HPC). Previous studies have shown that by varying the polymer blend ratio of the two polymers there exist a percolation threshold around 22 percentage of added HPC where bicontinuous structures are formed (Marucci, *et al*., 2009). In our work, we therefore choose to study phase separated polymer films being close to and above the percolation threshold.

The first type of material that has been investigated in this work is a model system, denoted as model polymer films. The model polymer films are produced by spraying a polymer solution onto a drum. Similar model EC/HPC films have been used in an extensive amount of previous studies and was therefore interesting as a starting material for our work (Frohoff-Hülsmann, *et al*., 1999). In this work, three model polymer films have been investigated and they contained 22 wt %, 30 wt % and 45 wt % of HPC, denoted as HPC22, HPC30 and HPC45.

The second type of material that has been investigated in this work is representative pellets where we study the internal structure of the coatings, denoted as polymer film coatings. In this study, microcrystalline cellulose cores were coated with a phase-separated polymer film in a fluidised bed. It should be noted that these pellets did not contain drugs. In this work, eight polymer film coatings have been investigated and they contained either 25 wt % or 40 wt % of HPC, denoted as HPC25 and HPC40. In addition the core diameters and the polymer film coating thickness were varied.

3.1 Model polymer films

The model polymer films were produced by spraying a polymer solution onto a rotating drum. In this work, three model polymer films have been investigated and they contained 22 wt %, 30 wt % and 45 wt % of HPC, denoted as HPC22, HPC30 and HPC45. In order to reveal the internal porous structure, the model polymer films were leached in water. The model polymer films are the material used in Paper I-Paper V.

3.1.1 Manufacturing

The model polymer films were produced by spraying an ethanol solution of ethyl cellulose (EC) and hydroxypropyl cellulose (HPC) on a hot rotating drum (Marucci, *et al*., 2009), see Figure 2. When the spraying procedure was finished, the films were peeled off the drum and stored in a desiccator. The thickness of the films was measured using the tool micrometer screw gauge. The measured film thickness was 133 μm for the HPC22 film, 159 μm and 150 μm for the HPC30 and HPC45, respectively. The film thickness is summarised in Table 1.

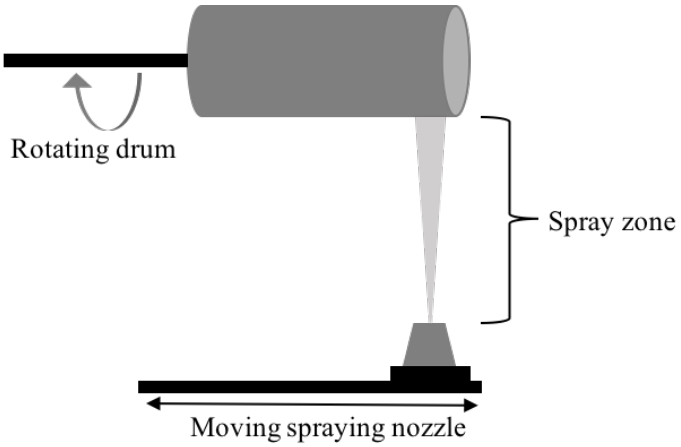

Figure 2. Schematic illustration of the manufacturing process of the model polymer films. The polymer solution was sprayed onto a rotating drum using a moving spraying nozzle.

3.1.1.1 Leaching of HPC

The water soluble HPC was dissolved by leaching the films in deionised water for 24 hours. The removal of HPC left a skeleton of EC with a porous network. The leaching of the films was done by cutting squares of 0.5 cm x 0.5 cm from the original films. The squared film samples were immerged in 700 ml stirred deionised water at room temperature for 24 hours. The deionised water was changed two times. Finally, the films were air-dried and later on stored in a desiccator. Figure 3 shows a sketch of leached porous film where the different features of the film are marked. The grey colour represents the EC matrix while the white represents the porous structure.

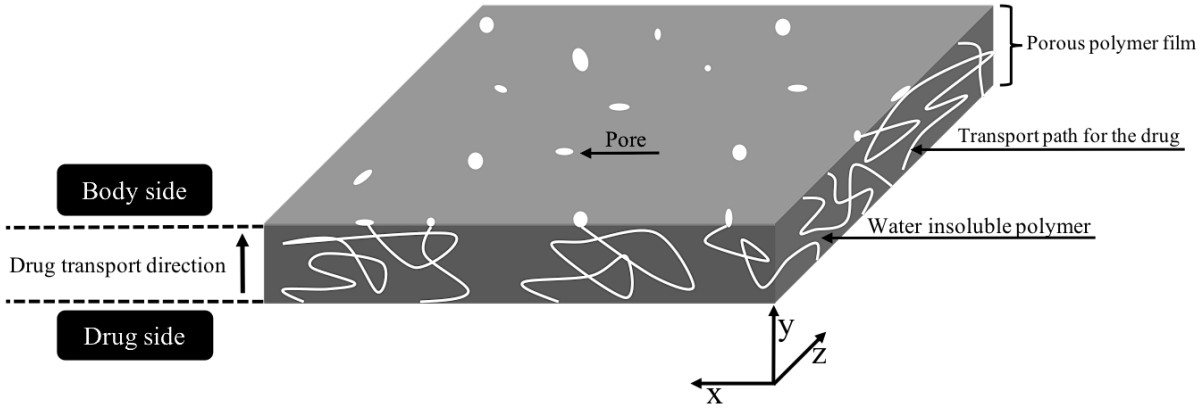

Figure 3. Schematic overview of the leached porous polymer film. The grey colour represents the porous ethyl cellulose (EC) matrix while the white represents the porous structure.

3.1.2 Composition

The microstructure of three model polymer films was studied. They contained 22 wt %, 30 wt % and 45 wt % of HPC, denoted as HPC22, HPC30 and HPC45 (EC: Ethocel™ Standard Premium 10 cps from Dow Wolff Cellulosic GmbH in Germany, HPC: Klucel® LF pharma grade from Ashland in USA). The total polymer content in the solution that was sprayed onto the rotating drum was 6 wt %. The polymer composition of the three model polymer films is summarised in Table 1.

Table 1. Model polymer films and their film composition and film thickness.

Sample	HPC weight fraction in film [wt%]	Film thickness [µm]
HPC22	22	133 µm
HPC30	30	159 µm
HPC45	45	150 µm

3.2 Polymer film coatings

The polymer film coatings were produced by coating microcrystalline cellulose cores with a polymer solution in a fluidised bed. In this work, eight polymer film coatings have been investigated and they contained either 25 wt % or 40 wt % of HPC, denoted as HPC25 and HPC40. In addition, the core diameter and the polymer film coating thickness was varied. The polymer film coatings were leached in water in order to reveal the internal structure. The polymer film coatings are the material used in Paper VI and Paper VII.

3.2.1 Manufacturing

The pellets, consisting of microcrystalline cellulose cores coated with polymer film coatings, were produced using the Wurster coating process which is a bottom spray fluidised bed technique. A schematic illustration of the Wurster coating process can be seen in Figure 4. A distributor plate, see black star (★), with a specific pattern of orifices determines the distribution of the hot fluidization airflow at the bottom of the tube. Spray nozzles, see black square (■), at the bottom supply a liquid solution containing the polymer blend as well as an atomization airflow that breaks the solution into droplets (●). The spray nozzles creates a spray zone (see number 1 in Figure 4) of the droplets which the microcrystalline cores (●) passes through in the Wurster tube (see number 2 in Figure 4). As the cores move around in the fluidised bed, the droplets dries in the fountain- downbed- and the horizontal regions (see number 3-5 in Figure 4) due to the hot airflow and finally a polymer film coating is formed.

The process conditions were kept constant and were as follows: The fluidizing gas was nitrogen with the inlet temperature of 80°C and gas flow 15 Nm^3/h. The nozzle diameter was 0.5 mm and the atomizer gas was nitrogen with the gas flow 0.54 Nm^3/h, the gas pressure 1.3 bar at a spray rate of 6.6 g/min. Coating time varied from 2.5 minutes (big core with thin coating) to 27 minutes (small core with thick coating).

The pellets consisted of a microcrystalline cellulose core that was either 270 µm (small core) or 666 µm (big core), coated with a phase-separated polymer film consisting of either 25 wt % or 40 wt % HPC and the coating thickness being either 10 µm (thin polymer film coating) or 40 µm (thick polymer film coating). The microcrystalline cellulose cores that were used for the small pellets were Celphere® 203 from Asahi Kasei Corp Japan and for the big pellets Vivapur® MCC spheres 500 from JRS Pharma GmbH Germany.

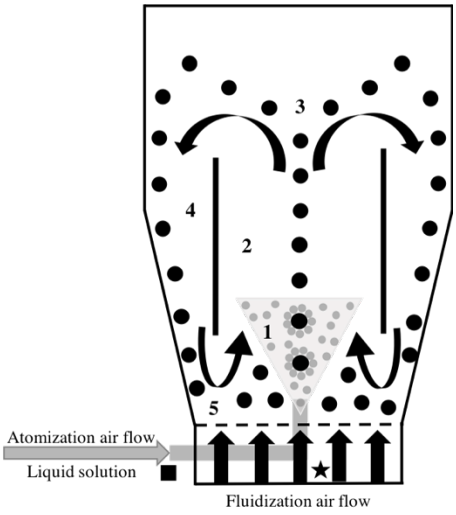

Figure 4. Schematic illustration of the Wurster coating process of pellets: 1) spray zone, 2) Wurster tube, 3) fountain region, 4) downbed region and 5) horizontal transport region.

3.2.1.1 Leaching of HPC

The polymer film coatings were later on leached in order to reveal the porous structure. The amount of HPC release was measured using a United States Pharmacopeia dissolution apparatus (Agilent, Switzerland) equipped with a paddle. Figure 5 shows a sketch of a leached polymer film coating on a pellet where the different features of the coating are marked. The grey colour represents the EC matrix, white represents the porous structure and black represents the core.

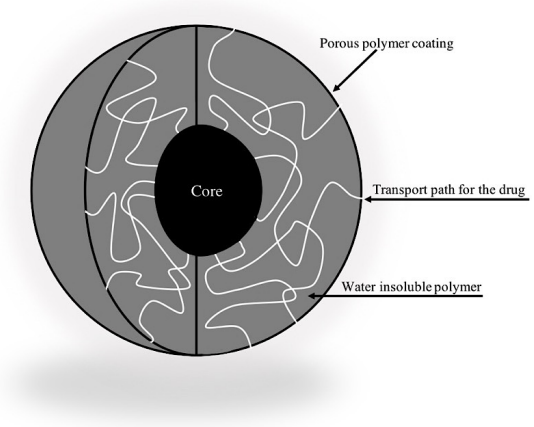

Figure 5. Schematic overview of a leached polymer film coating on a pellet. The grey colour represents the porous ethyl cellulose (EC) matrix while the white represents the porous structure.

3.2.2 Composition

For each type of pellet, 10 g of microcrystalline cellulose spheres were coated with an ethanol solution of EC and HPC in a bottom spray fluidized bed (Mini-Glatt micro-kit retrofitted, Glatt GmbH). The ethanol was 95% v/v from Kemetyl AB, Sweden, ethyl cellulose was Ethocel® with standard premium viscosity grade 10 cP from Dow Wolff Cellulosics GmbH, Germany and the hydroxypropyl cellulose was from Klucel® HPC LF Pharm from Ashland Inc. USA. The total polymer concentration was the same in all polymer film coating trials, 6.0 wt % and the amount of HPC in each experiment and target coating thickness is shown in Table 2.

Table 2. Pellet samples and their film composition and target coating thickness.

Sample	Microcrystalline cellulose core	HPC weight fraction in film [wt%]	Target coating thickness [μm]
Small HPC25 thin coating	Celphere® 203	25	10
Small HPC25 thick coating	Celphere® 203	25	40
Small HPC40 thin coating	Celphere® 203	40	10
Small HPC40 thick coating	Celphere® 203	40	40
Big HPC25 thin coating	Vivapur® 500	25	10
Big HPC25 thick coating	Vivapur® 500	25	40
Big HPC40 thin coating	Vivapur® 500	40	10
Big HPC40 thick coating	Vivapur® 500	40	40

Chapter 4
Characterisation methods

4.1 FIB-SEM dual beam microscopy

A focused ion beam (FIB) combined with a scanning electron microscope (SEM) provides the possibility to reveal and image the internal structure of materials. The FIB-SEM has one ion column and one electron column, where upon the ion and electron beams are focused separately during vacuum conditions. The FIB-SEM utilises the focused ion beam to make cross-sections with high precision and the electron beam to image the internal structure with high spatial resolution (Bassim, *et al*., 2014; Cantoni, *et al*., 2014; Moghadam, *et al*., 2006).

The FIB-SEM instrument utilised throughout this work was a Tescan GAIA3 (Tescan, Czech Republic). The FIB-SEM tomography software from Tescan was utilised to perform the slice and image procedure. The instrument was equipped with a gas injection system (platinum and carbon). The coincidence point of the ion and electron beam was at 55° and the working distance was 5 mm, see Figure 6 for the FIB-SEM setup.

In Paper I, we present a protocol for the optimisation of FIB-SEM tomography parameters for porous and poorly conducting soft materials. The protocol reduces cross-sectioning artefacts, charging and eliminates shadowing effects. These commonly encountered challenges during FIB-SEM tomography are explained in detail in the following sections.

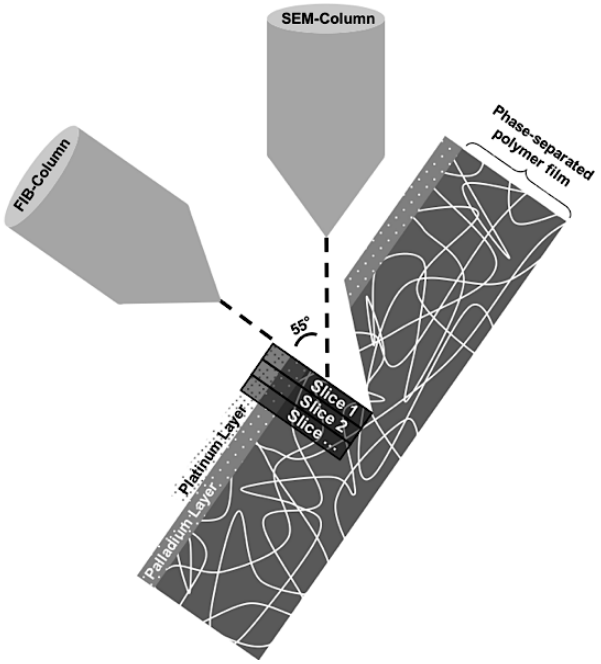

Figure 6. A schematic showing the geometry setup in the FIB-SEM of the focused ion beam, the electron beam and the sample. The incident angle on the sample of the electron beam and the ion beam is 90˚ and 55˚, respectively, in order to perform milling an imaging without sample tilting in between.

4.1.1 Ion beam milling

Ions can be utilised for removing material from a sample, depositing material onto the sample as well as imaging the sample surface with high spatial resolution and precision. However, ions are significantly more massive compared to, for example, electrons, which thus needs to be kept in mind when imaging with ions. Imaging with ions may sputter material away and thus damage the sample surface (Giannuzzi, *et al*., 2005). A sputtering process occurs if the kinetic energy of the ions is sufficient to overcome the surface binding energy of the atoms in the sample. Figure 7 shows a schematic illustration of the interaction between an ion and the sample surface (Nastasi, *et al*., 1996). This sputtering process is referred to as milling in the literature. The milling process can be controlled, hence be performed with high precision (Giannuzzi, *et al*., 2005).

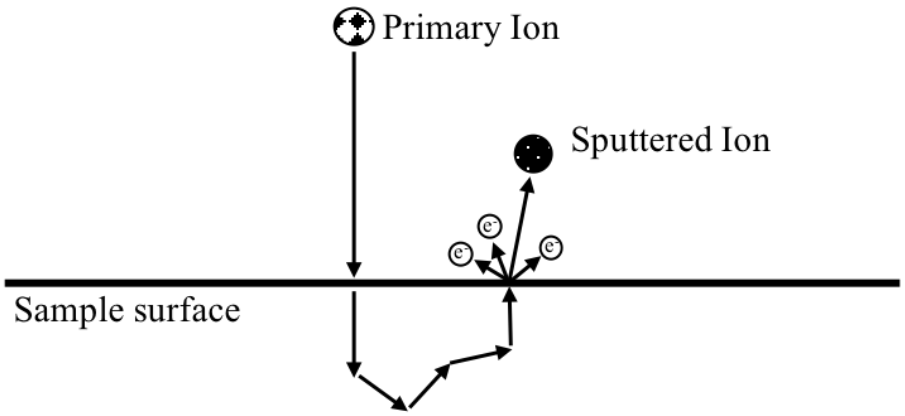

Figure 7. Schematic illustration of ion-solid interaction between an incident ion and a sample surface resulting in a sputtered ion from the sample (adapted from Nastasi, *et al*., 1996).

4.1.1.1 Cross-sectioning artefacts

Ion beam milling can cause artefacts such as curtaining or redeposition during the preparation of a cross section (Giannuzzi, *et al*., 2005). It has been shown that these artefacts can be reduced by fine-tuning the ion beam current and energy (Walley, *et al*., 1971; Suzuki, 2002; Drobne, *et al*., 2007). Curtains are vertical lines seen in the cross-section surface caused by the ion beam. Different hardness within a material or thickness can cause different ion milling rates which can cause curtaining. Redeposition is removed material that is still in the chamber and redeposit onto the cross-section surface. Previous work has shown that deposition of a platinum coating on the surface of the sample can be used to reduce the curtaining effect (Walley, *et al*., 1971; Suzuki, 2002; Drobne, *et al*., 2007). A platinum gas precursor is then injected into the chamber. The precursor is cleaved by the ion beam and this results in deposition of platinum on the sample under the ion beam. The platinum coating provides a homogenous surface which give rise to a more constant milling rate. It has also been shown that curtaining and redeposition can minimised by reduced milling rates (Giannuzzi, *et al*., 2005).

4.1.2 Electron beam imaging

Electrons can be utilised to image as well as deposit material onto the sample surface. The incident electrons interact with the sample surface which results in an interaction volume, see Figure 8. This interaction produces different signals that can be detected with suitable detectors for the different signals (Goldstein, 2003). The signals are, for example, backscattered electrons, secondary electrons and characteristic X-rays. Figure 8 shows a schematic of the interaction volume and different types of signals. The backscattered electrons are produced

when a primary electron interacts with an atom in the sample. The interaction causes the path of the primary electron to deviate from its original path and leave the sample as a backscattered electron. The secondary electrons result from inelastic scattering of the primary electrons giving rise to the emission of electrons from the atoms in the sample. Characteristic X-rays are produced when the empty state created by an emitted electron is filled with an electron from a higher electron energy shell. The energy difference between the two shells gives the energy of the characteristic X-rays.

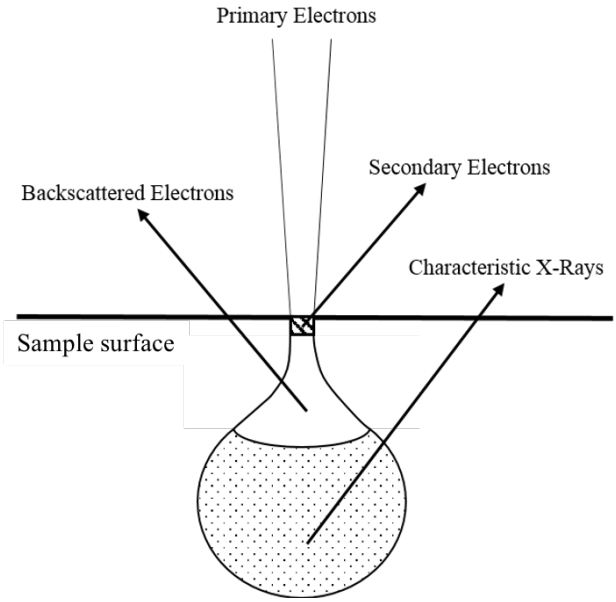

Figure 8. Schematic illustration of the interaction between the electron beam and the sample (adapted from Goldstein, 2003).

4.1.2.1 Imaging challenges

Two common problems encountered when imaging a cross-section surface utilising an electron beam are shadowing-effects and charging. The shadowing-effects are caused by the surrounding material of the cross section. In order to eliminate these shadowing-effects, trenches on each side and in front of the cross section (a U shape) can be milled with the ion beam (Holzer, *et al*., 2004). Figure 9 shows a schematic overview of the different steps involved to establish the U shape. The initial step was to deposit a thin platinum coating on the sample surface to reduce the curtaining effect. The platinum deposition was done within two steps, first by deposition with the electron beam and then by the ion beam, Figure 9 (number 1). A cross section was milled in order to reveal the internal porous structure, Figure 9 (number 2), followed by milling narrow trenches on each side of the cross section, Figure 9 (number 3). In order to

reveal the full cross-section surface, a bigger trench in front of the cross-section was milled, Figure 9 (number 4). Subsequently, platinum was deposited in two squares where fiducial markers (used to drift compensation) was milled into, Figure 9 (number 5). The last step was to clean the cross section from curtains and redeposition, Figure 9 (number 6). This was also the starting point of the slice and image procedure.

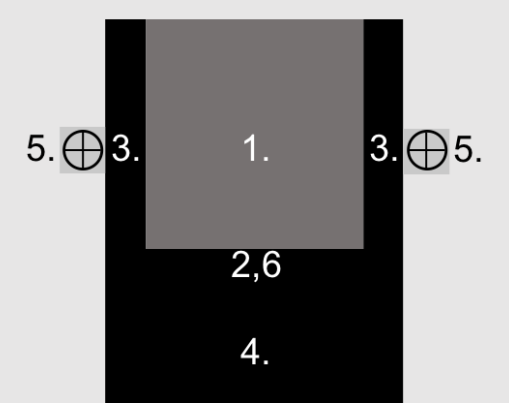

Figure 9. Schematic overview that shows the different steps required to establish a U shape. Number 1 represents deposition of a protective platinum coating. Number 2 shows the location of the first cross-section of the U shape. Number 3 represent the narrow trenches of the U shape. Number 4 shows the big trench that revealed the full cross-section surface. Number 5 shows the location of the fiducial markers for the FIB and the SEM. Number 6 is the starting point of the slice and imaging procedure.

From previous findings, it is known that no charging of poorly conductive materials is present when the number of primary electrons impinging on the surface is roughly equal to the number of electrons emitted from the sample surface, i.e. the total number of backscattered electrons (BSE) and secondary electrons (SE) (Goldstein, 2003). The beam energy influences the ratio between the number of incoming electrons and the emitted electrons and therefore needs to be tuned to achieve the condition of no charging. There are two cross-over points, E_1 and E_2, where the primary beam energy gives an electron yield equal to 1. For soft materials, the low energy cross-over point occurs in the energy range of 0.5 keV – 2 keV and the high energy cross-over point at 2 keV - 5 keV (Goldstein, 2003). At low energy below the first cross-over point, E_1, there is a negative charge accumulation. At energies between the two cross-overs there is a positive charge accumulation and above the second cross-over point, E_2, there is a negative charge accumulation.

Furthermore, when imaging conducting materials with low electron beam energy, a secondary electron detector is often selected (Goldstein, 2003). However, when charging occurs, the secondary electrons are much more affected by the charging because of their low kinetic energy, < 50eV than backscattered electrons. Therefore, BSE is preferred when imaging poorly conducting materials.

Another approach to reduce charging while imaging poorly conducting samples with electrons is to operate the FIB-SEM in a low-vacuum condition. It reduces charging through ionisation of the gas molecule. The ions neutralise the accumulated charges at the surface (Robinson, 1975; Moncrieff, *et al*., 1978; Stokes, 2008). This approach can however not be used simultaneously with the ion beam. It has also been shown that a localised discharge can be achieved by injecting a nitrogen gas using a gas injection system (Schulz, *et al*., 2009). This approach limits the volume of lower vacuum and the area of interest can be imaged with reduced charging.

As already mentioned, porous and poorly conducting soft materials have to be prepared before they can be inserted into the FIB-SEM for tomography. Previous work has shown that an increase of the concentration of heavy metals, for example osmium, in the sample reduces charging (Seligman, *et al*., 1966; Tanaka, *et al*., 1984; Deerinck, *et al*., 2010). The heavy metals increase the conductivity of the poorly conductive samples. In addition, it has been shown that a combination of low electron beam energy, osmium-fixed samples and backscattered electron detector can be used to image poorly conductive samples. The low electron beam energy reduces the charging and the osmium-fixation enhances the contrast as well as increases the BSE yield (Harris, *et al*. 1976; Holzer, *et al*., 2004; De Winter, *et al*., 2009).

4.2 Data segmentation

3D reconstruction of materials using FIB-SEM tomography is done by reconstructing binary 2D image stacks. Binarisation of the 2D image stacks are usually performed by aligning the image stack, followed by cropping and segmentation (Jorgensen, *et al*., 2010; Salzar, *et al*., 2012). Global thresholding is one common way to perform the segmentation (Efford, *et al*., 2000). In global thresholding, a prechosen threshold value is determined to distinguish the two phases. If the grey level value of a pixel is below the prechosen threshold, it belongs to one of the phases and if it is above, it belongs to the other phase. However, the segmentation of porous materials is complex. The 2D image of the cross-sections does not only contain information about the cross-section surface but also subsurface information from inside the pores (Zils, *et*

al., 2010; Schulenburg, *et al*., 2011). This leads to overlapping intensities where global thresholding is not sufficient as segmentation method. Even more advanced segmentation algorithms such as local thresholding have been presented but does not solve this complex segmentation problem (Blayvas, *et al*., 2006; Thiedmann, *et al*., 2011).

In Paper II, a method based on machine learning was developed and utilised to segment the FIB-SEM tomography data on porous and poorly conducting polymer films. A so-called random forest classifier was trained to perform classification into one of two possible classes, pore or solid (Breiman, 2001). Manual segmentation was performed in 100 randomly placed square regions of size 256x256 pixels in each data set which was used to train the algorithm. The algorithm was later on utilised to successfully segment three different data sets.

4.3 Quantified characterisation of porous networks

Quantitative pore parameters that have been used for describing porous networks in our work are, for example, pore size distribution, pore morphology, interconnectivity and tortuosity. Under some conditions, pore size and pore morphology can be estimated from 2D data (Markl, *et al*., 2018)., but in order to extract information about interconnectivity and tortuosity, 3D data is crucial. It is important to quantify the characteristics of a porous network in a material in order to understand what gives rise to the transport properties in porous materials.

In Paper III and IV we determine pore size distribution, pore morphology, interconnectivity and tortuosity on model polymer films. The methods utilised in Paper III and IV are briefly described in the following sections.

4.3.1 Pore morphology and pore size distribution

Total porosity and spherical pore size distribution are frequently used characterisation methods (Markl, *et al*., 2018). However, these measures do not give any information about anisotropy. In Paper IV, we investigated the pore morphology and pore size distribution with respect to simple objects in 1D, 2D and 3D. The objects were lines in different directions (1D), circles in different planes (2D) and spheres (3D). The 3D reconstructions provided the possibility to characterise the pore morphology in 3D where the lines were oriented in 11 directions, circles oriented in the xy-, xz- and yz-planes, and spheres. In order to extract the information about the pore morphology in 3D, the simple objects were fitted into the porous network. Lines and circles gives information about anisotropy of the porous structure.

4.3.2 Quantification of interconnectivity

The interconnectivity of porous networks strongly influences the transport properties and it is therefore important to quantify the interconnectivity and correlate it to the transport properties of porous material (Armatas, 2006; Vogel, 1997; Ghassemzadeh & Sahimi, 2004; Yang, *et al.*, 2014). There are many different ways to quantify 3D porous networks. For example, helium pycnometry and mercury porosimetry fill the porous network by gas or liquid to assess the pore volume in the sample (Ferrero, *et* al., 2002; Westermarcka, *et* al., 1999). However, we cannot visualise the interconnectivity and the tortuosity of the porous network by using these techniques.

In Paper III, we use mathematical tools, namely geodesic paths, channels and tortuosity, to visualise and quantify the interconnectivity of porous networks.

4.3.2.1 Individual through paths

Interconnectivity of a porous network can be visualised by geodesic paths. A geodesic path, denoted by GeoPath(p), is defined in this context as the shortest path that satisfies the following three constraints: (1) it starts at a chosen inlet-pore, (2) it ends anywhere at the outlet surface and (3) it passes through point p. Choosing different points p thus gives different shortest geodesic paths. This is illustrated in Figure 10 where a 2D porous network is shown with three different points p and their corresponding geodesic paths from the same inlet-pore.

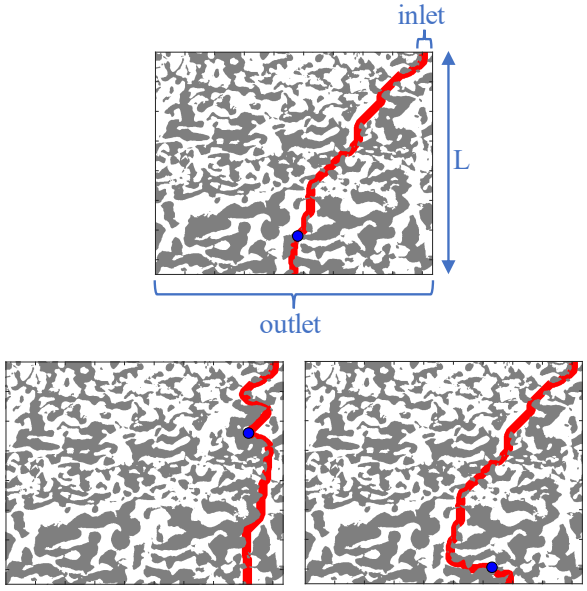

Figure 10. Illustration of geodesic paths, GeoPath(p) (marked in red), for different points p (marked in blue). The inlet (top) and outlet (bottom) are marked in the top figure. The height of the porous network is L.

4.3.2.2 Limiting Layer

In order to capture important features of the porous network, information about connections in the network, i.e. where many paths coincide, so-called geodesic channels were computed and quantified. Figure 11 shows an example of the geodesic channel measure computed in the same 2D porous network from Figure 10. The main channels, i.e. the channels of high strength, are the most important paths connecting the 2D porous network with the chosen inlet and outlet. The quantification of channels enables identification of for example limiting layers containing only a few main channels.

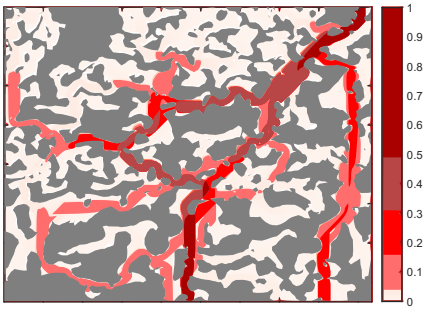

Figure 11. Illustration of geodesic channels with the same inlet and outlet as in Figure 10. The colourbar indicates the strength of the geodesic channel. Only pores that are connected to both inlet and outlet are visible.

4.3.2.3 Tortuosity

There exist different types of tortuosity, such as hydraulic, electrical and diffusive tortuosity, which can be computed from fluid or diffusion measurements or simulations (Berg, 2012; Ghanbarian, *et al.*, 2013; Julbe & Ramsay, 1996; Veroort & Cattle, 2003; Vogel, 1997). Geodesic tortuosity has previously been used to predict diffusive transport with good results (Stenzel, *et al.*, 2016; Barman, *et al.*, 2018). The geodesic tortuosity is defined as the length of a geodesic path divided by the thickness of the porous network (Peyrega & Jeulin, 2013).

In order to quantify the tortuosity of porous networks, the tortuosity values, i.e. the relative lengths of the geodesic paths were computed. The tortuosity measures how much longer the geodesic path is compared to the distance between the inlet and the outlet and therefore indicates how tortuous the path is.

4.4 Mass transport

Diffusive transport is driven by random movement of particles, where each particle moves according to Brownian motion. The diffusive flux J gives the net amount of particles transported per unit area and time. The directions are x, y and z which gives that $\mathbf{J} = (J_X , J_Y , J_Z)$. The net amount of particles transported in the x-direction per unit area and time is the J_X while the J_Y and J_Z is the net amount transported in the y-and z-direction. Equation 1 shows that **J** is proportional to the negative concentration (c) gradient in all three directions ($\nabla = (\frac{\partial}{\partial x}, \frac{\partial}{\partial y}, \frac{\partial}{\partial z})$) and where D_0 is the diffusion coefficient.

$$\mathbf{J} = -D_0 \nabla c \qquad \text{(eq. 1)}$$

The random movement of particles results in a net transport of particles from regions with higher concentration to regions with lower concentration. The mass conservation law implies that the rate of change($\frac{\partial c}{\partial t}$) should be equal to $\nabla \cdot \mathbf{J}$ for constant D_0 and this results in equation 2.

$$\frac{\partial c}{\partial t} = -D_0 \Delta c \qquad \text{(eq. 2)}$$

The diffusive transport rate through a porous material is determined by its pore geometry. Previous work have shown that there are two additional pore geometry-properties that are thought to be important for determining the rate of diffusive transport through porous structures. The two additional pore-geometry properties are the length of paths through the porous structure and possible bottleneck effects (Siepmann, *et al*., 2012), i.e. long paths and/or the presence of bottlenecks can cause low transport rates.

4.4.1 Simulated diffusion

Several methods may be used for computation of mass transport properties. Here, the lattice Boltzmann method (Gebäck, *et al.,* 2015; Krüger, *et al*., 2017), which is often used for mass transport simulation in porous media, has been utilised.

In order to compute the effective diffusion coefficient of the porous networks in Paper V, the lattice Boltzmann method (Gebäck, *et al*., 2014; Ginzburg, *et al*., 2005) was employed to solve the diffusion equation. The effective diffusion coefficient describes diffusion through the porous network.

4.4.2 Experimentally measured diffusion

The effective diffusion coefficient for model polymer films was calculated from permeability measurements performed using a diffusion cell. The diffusion chamber consisted of two chambers separated by the film to be investigated. A circular film segment was cut out of the model polymer film, and the thickness was measured with a micrometer screw gauge. The piece of the film was then placed between the two cell compartments. At the beginning of each experiment, 15 mL of deionized water was added to both cell compartments simultaneously, to avoid any pressure on the membrane. After 15 min, a small amount of tritiated water was added to the donor compartment, and two paddles were used to stir the water. Samples were taken from the receiver compartment at specified time intervals and replaced by the same amount of pure distilled water. The increase in tritium activity in the receiver compartment was divided by the tritium activity per unit volume in the donor cell and finally the effective diffusion coefficient of the model polymer film could be calculated (Lindstedt, *et al*., 1989).

Chapter 5
Results and discussions

5.1 Optimisation of ion beam milling and electron beam imaging

3D reconstruction of porous structures of materials by serial sectioning using a FIB-SEM is a well-established procedure. However, beam sensitive and poorly conducting materials are challenging. The electron beam may give rise to accumulation of charges at the surface due to poor electrical conduction and cause image distortion. Another challenge is that the ion beam can destroy the sample by surface melting, ion beam damage or induce curtaining effects (Giannuzzi, *et al*., 2005). These challenges have been addressed in Paper I and are descried in the following sections.

5.1.1 Reduction of curtaining during ion beam milling

Curtains are vertical lines seen in the cross-section surface caused by the ion beam. We have reduced the curtaining effect by optimising the ion-beam parameters as well as depositing a protective platinum layer on the region of interest.

5.1.1.1 Optimisation of ion beam parameters

Curtaining can be minimised, for example, by reduced milling rates (Giannuzzi, *et al*., 2005), where parameters that affect the milling rates are ion-beam energy and current. We chose to start the optimisation procedure at 30 kV which is a standard operation voltage for preparation of cross sections. The results showed that the cross-sectioning artefacts could all be avoided at 30 keV. The current was optimised by the following experimental approach. When milling the largest trench in the formation of the U shape, a current as high as possible without causing cross-sectioning artefacts was required in order to achieve time-efficient milling. The tuning of the high beam current for the initial stage started at a value of 20 nA followed by a stepwise increase to find the optimised current, in our case 40 nA. Cross-sectioning artefacts resulted from the relatively high beam current. However, these were removed in subsequent polishing of the cross section where lower beam currents were used. The other milling operations were optimised using the same approach, but starting at lower currents. The surface morphology was examined after each milling to find the highest current that did not cause cross-sectioning

artefacts. In this study, the optimised ion-beam parameters for slicing and polishing were 1 nA and 30 keV.

5.1.1.2 Deposition of protective layer

Previous work has shown that deposition of a protective platinum layer onto the sample can reduce the curtaining effect (Mayer, *et al*., 2007). In addition to platinum precursors, other gas precursors such as tungsten or carbon are available on our FIB-SEM system. These layers are deposited by electron or ion beam induced deposition in situ. An additional layer to reduce charging can be deposited ex situ prior to the work in the FIB-SEM. Figure 12a shows a BSE SEM cross sectional image where a few nanometre thin palladium layer has been deposited ex situ. The arrows in Figure 12a points to curtains caused by the ion beam. It can also be seen that the top surface of the polymer film is smeared. Figure 12b shows a cross section with the palladium layer, and a subsequent protective carbon layer. The arrow points to the interface between the protective layer and the top surface of the polymer sample. Figure 12c shows a cross section with palladium layer and tungsten as protective layer and in Figure 12d the protective layer deposited on top of the palladium layer is platinum. The smearing of the polymer sample observed in Figure 12a is absent in Figures 12b-d. As can be seen, the different protective layers gives different contrast compared to the polymer sample. One advantage of the distinct contrast difference between the sample and the protective layer is that it simplifies the image alignment procedure. The optimal protective layer to deposit depends on the material that is to be analysed. For the case of both the model polymer films and the polymer film coatings, the optimal layer combination for charge reduction and protection was found to be a combination of palladium and platinum, Figure 12d, due to reduction of curtaining as well as distinct contrast between the top surface of the polymer sample and the platinum layer. In this work, an Emitech K550X Palladium Sputter (Quorum Technologies Ltd, Ashford, United Kingdom) was used with the coating current of 25 mA for 15 minutes while rotating the sample holder.

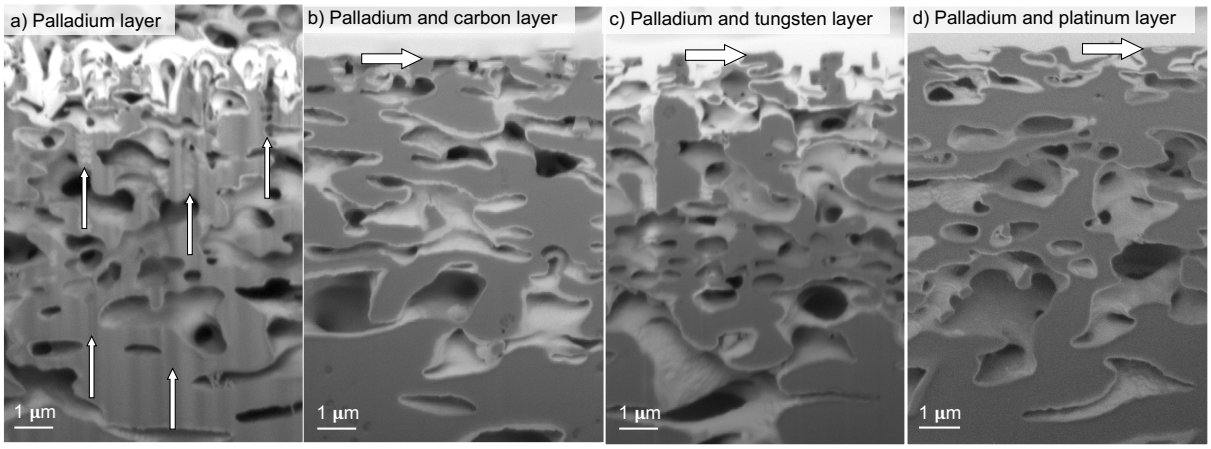

Figure 12. SEM BSE images showing cross sections of a soft porous polymer sample with different protective layers: (a) Charge-reducing palladium layer has been deposited, curtaining effect is highlighted by arrows. The top surface of the polymer sample is also smeared. (b) Palladium layer and protective carbon layer, c) palladium layer and protective tungsten layer, and d) palladium layer and protective platinum layer. Arrows in b)-d) point to the interface between the protective layer and the top surface of the polymer sample. The smearing observed in a) is absent in b)-d).

5.1.2 Reduction of charging during electron beam imaging

The electron beam used for imaging may give rise to accumulation of charges at the cross section surface due to poor electrical conduction and cause image distortion. We have reduced the charging effect by optimising the electron-beam parameters, selection of detector as well as charge neutralisation using carbon gas which are explained in the following sections.

5.1.2.1 Optimisation of electron beam parameters

The first step to reduce charging during imaging was done by fine-tuning the electron-beam parameters. This was carried out by varying the energy until as little charging as possible was noticed while sustaining sufficient detector signal. The initial electron beam energy was chosen to be 2 keV, based upon the rule of thumb that the primary beam energy for no charging of poorly conducting materials lies within 0.5 keV – 2 keV, depending on the material (Goldstein, 2003). Different electron beam energies were applied to find the optimised electron beam energy for imaging soft poorly conducting materials, see Figure 13. Using this empirical approach, the optimised electron-beam energy was found to be 700 eV, see Figure 13b. If the electron beam energy was below 700 eV, less charging was observed. However, too poor signal was received giving insufficient signal/noise ratio, see Figure 13a. If an electron beam energy

above 700 eV was selected, the signal was improved, see Figure 13c-h. However, accumulation of local charges was observed. The accumulation increased with decreasing scan rate and progression of time for the slice-and-image session. The next step was to optimise the electron beam current, which was achieved with the same approach as for the electron beam energy. The optimised current corresponded to the minimum available current in the instrument settings, which was 10 pA. Figure 14 shows results for the different beam currents that were evaluated to find the optimal value.

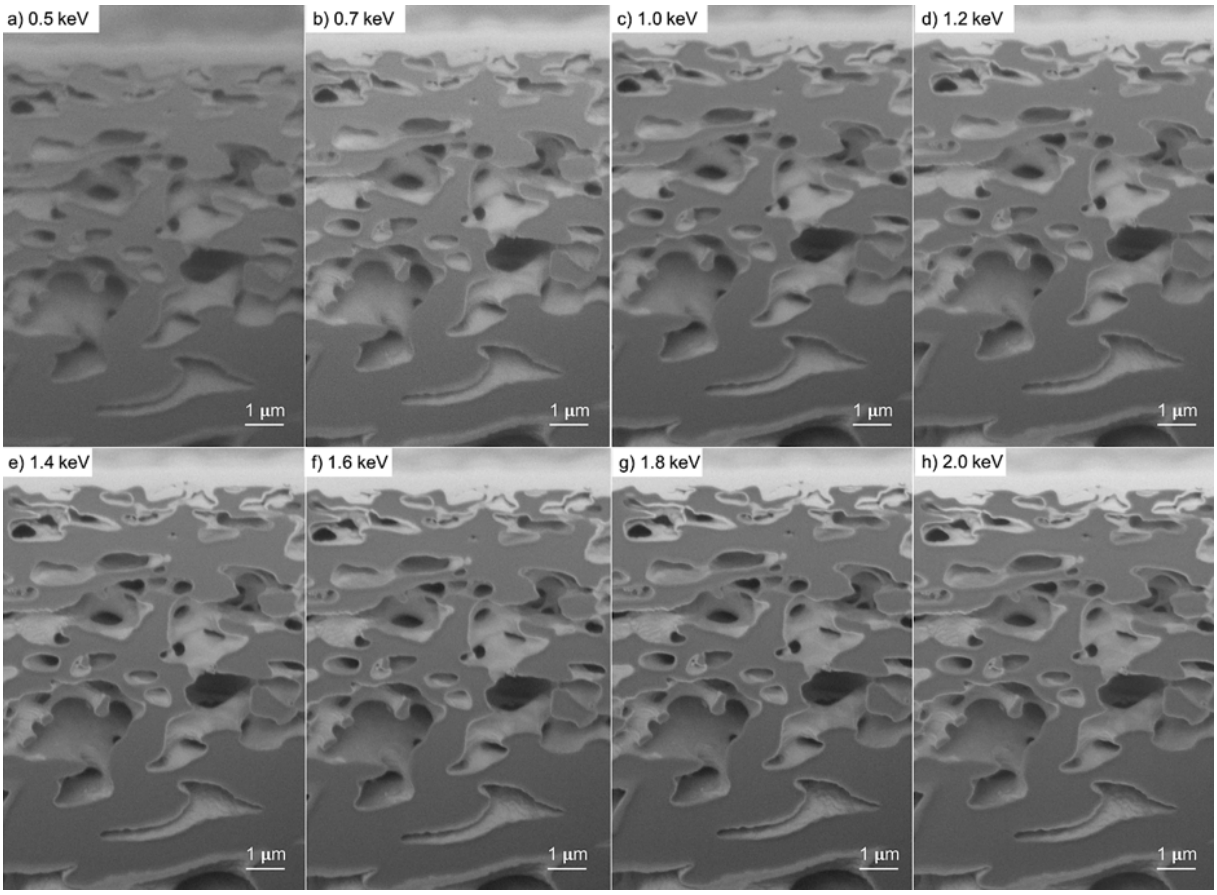

Figure 13. SEM BSE images illustrating the procedure used for selecting the optimised electron beam energy. Images recorded at energies ranging from (a) 0.5 keV to (h) 2 keV. The electron beam current was kept constant at 10 pA. The optimal electron beam energy was found to be 700 eV based both on the individual images and the accumulation of charge during the slice-and-image session.

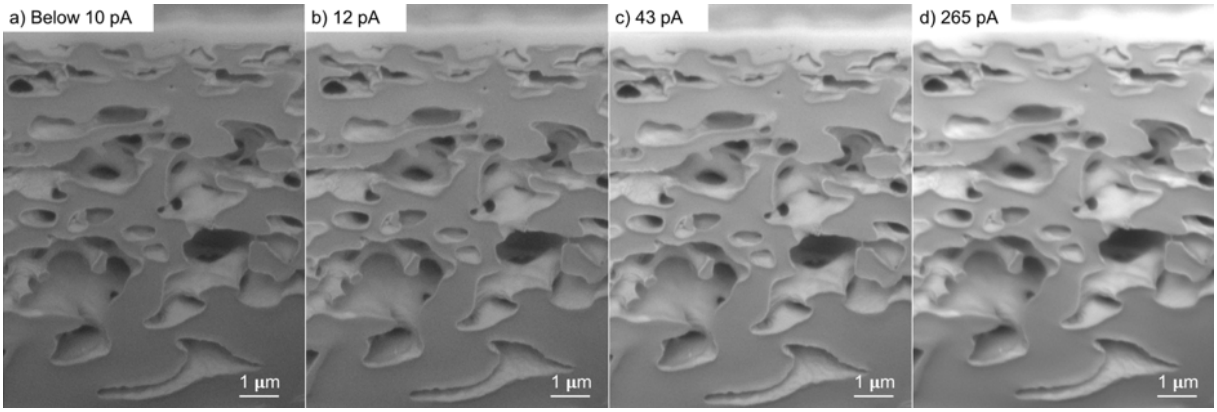

Figure 14. SEM BSE images illustrating the procedure for selecting electron beam current, ranging from (a) below 10 pA to (d) 265 pA. The electron beam energy was kept constant at 700 eV. The optimal current corresponded to the minimum beam current that could be used, which was 10 pA.

5.1.2.2 Selection of detector

The second step to further reduce charging was to select the detector. Secondary electron detector is often selected when imaging conducting materials with low electron beam energy (Goldstein, 2003). However, when charging occurs, the secondary electrons (SE) are much more affected because of their low kinetic energy, less than 50eV, compared to backscattered electrons (BSE). Thus, BSE are preferred when imaging poorly conducting materials. Figure 15a shows a cross section imaged using a SE detector where the arrows point to local charged areas. The same areas can be seen in Figure 15b without charging when imaged with the BSE detector. It should also be noted that the pore edges can more clearly be distinguished in the BSE image.

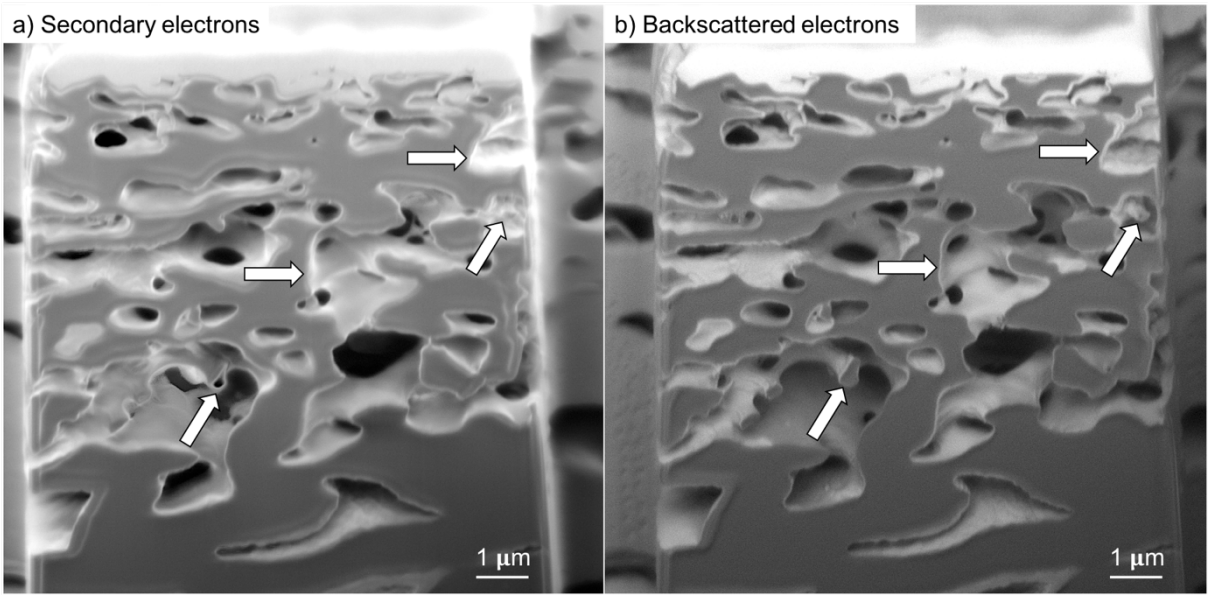

Figure 15. a) Cross section imaged using the SE detector where the arrows are pointing to locally charged areas. b) Cross section imaged using the BSE detector where the arrows are pointing to the same areas as in a) but without charging.

5.1.2.3 Charge neutralisation

The final step to reduce charging even further was to inject carbon gas prior to imaging. Figure 16a shows effects of charging and Figure 16b shows when charge neutralisation using the insertion of a carbon gas has been utilised resulting in no observable charging. Cross-sectioning artefacts were present when carbon gas was injected during milling. Hence, the gas was only injected prior to the electron-beam imaging. The charge neutralisation procedure was carried out as follows: Carbon gas was injected into the chamber for 5 seconds by opening the carbon gas valve. The valve was closed after 5 seconds whereupon imaging with reduced charging could be performed. This procedure was incorporated in the automatic slice-and-imaging procedure by pausing after each slicing. Therefore, the slice-and-imaging procedure resulted in a semi-automatic procedure. It was found that the distance between the sample and the valve opening played an important role. If the valve opening was too close to the sample surface, carbon deposition occurred. If the valve opening was too far away from the sample surface, no charge neutralisation occurred. The optimised distance between the valve opening and the sample surface was experimentally identified. The gas-injection system (GIS) was first inserted to its end position and by retracting the GIS for 10 seconds, the optimised distance was achieved.

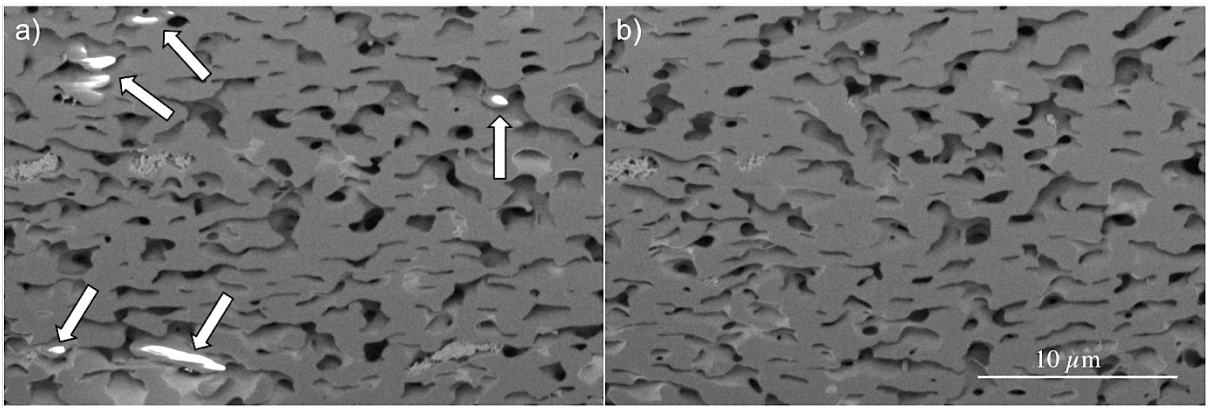

Figure 16. a) SEM BSE cross sectional images of a porous polymer sample with charging where arrows indicate on the locally charged areas. b) SEM BSE image of a cross section where charge neutralisation using carbon gas has been used and no charging is observed.

5.2 3D visualisation

FIB-SEM tomography, where ions are used to perform serial sectioning and the electron beam is used to image the cross-section surface, has been utilised to acquire high spatial resolution 3D data on soft, porous and poorly conducting materials. The 3D structure of two different types of samples, model polymer films (Paper I) and polymer film coatings on microcrystalline cellulose cores (Paper VII) with different porosities, have been successfully reconstructed.

5.2.1 Practical aspects

In order to investigate the internal structure of the model polymer films as well as the polymer film coatings, the samples were mounted on an alumina stub attached using an adhesive carbon tape. Deposition of a thin palladium layer onto the sample surfaces was done to reduce charging effects. Figure 17 shows the FIB-SEM tomography setup for pellets where Figure 17a) shows the pellet with the FIB view and Figure 17b) with the SEM view.

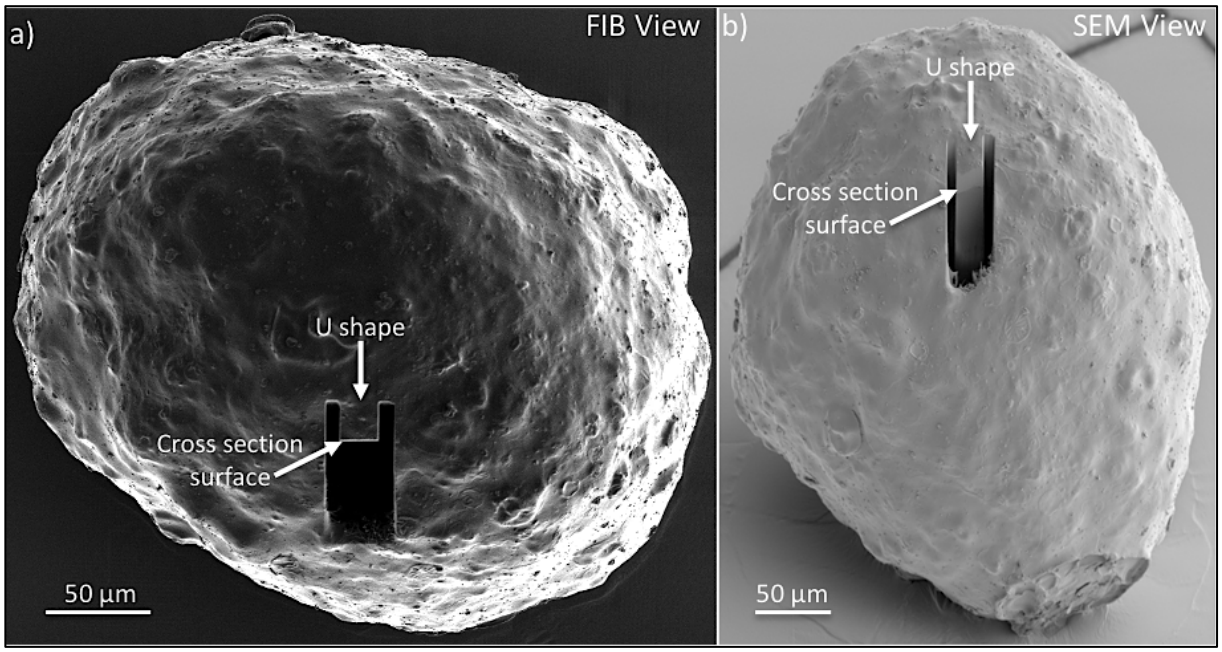

Figure 17. The FIB-SEM tomography setup for pellets where a) ion beam SE image shows the FIB view and b) SEM BSE image shows the SEM view. The U shape and the cross section surface are marked with white arrows in both images.

In order to acquire high spatial resolution 3D data on poorly conductive materials, utilization of drift correction is preferred to prevent potential drift during ion milling that can lead to destroying the created U shape. Figure 18 shows an overview of a U shape with platinum deposited on top and in a) before the automatic slice and image procedure started and in b) after the slice and image procedure was finished. In Figure 18a-b, a white triangle marks the cross sectional surface (△), a filled circle the fiducial maker etched into a square of deposited platinum (◉) and a star (☆) on the same position in a) and b). From Figure 18b) it can be seen that the ion beam started to mill in the middle of the U shape, see the position of the star (☆) in a) and in b). It was observed that the software did not recognize the fiducial marker in b) (see the circle (◉)) after approximately 30 slices due to prior to each slice, an ion beam image was

acquired on the fiducial maker resulting in etching and stepwise removal of the fiducial marker. The tomography data on polymer film coatings was acquired in sub-sequential steps, i.e. 30 images were acquired followed by a restart of the slice-and-image procedure including imaging a new fiducial marker.

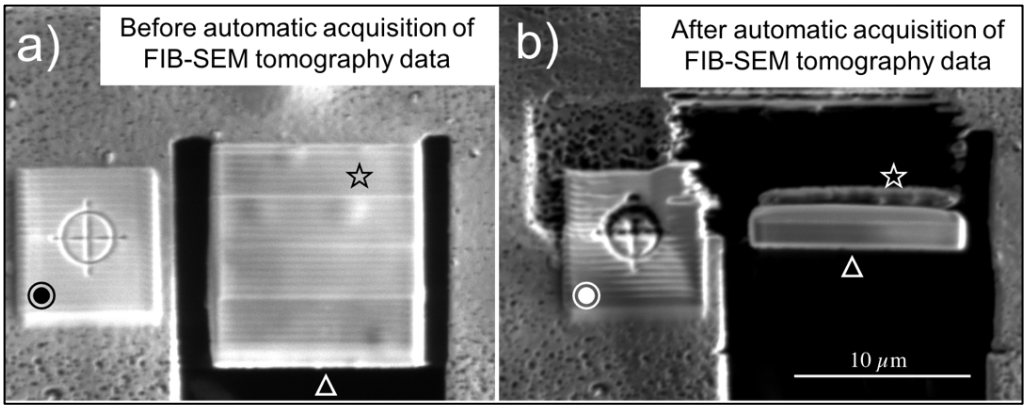

Figure 18. Ion beam SE images of the U shape when drift problem is observed where a) is before automatic acquisition of FIB-SEM tomography data and b) is after automatic acquisition of FIB-SEM tomography data.

5.2.2 Model polymer films

The FIB-SEM tomography data on model polymer films were acquired using the protocol for optimisation of FIB-SEM parameters explained in the previous section 5.1. The 2D image stacks were obtained by using the ion beam for serial sectioning with the slice thickness 50 nm for 10 μm depth (z). The width of the cross-section was 45 μm and the height 35 μm. The ion-beam parameters used for slicing were 1 nA and 30 keV. The cross section surface was imaged utilising a mid-angle BSE detector with scan speed 2 μs/pixel and 10 nm pixel size. The electron beam parameters used for imaging was 700 eV and 1 pA. The 200 sequential 2D images were aligned and cropped using the software ImageJ (Schneider, *et al*., 2012) and finally segmented using a self-learning segmentation algorithm. From the automatic segmented data, the pore volume was determined to be 20 % for HPC22, 32 % for HPC30 and 44 % for HPC45. The obtained porosities are in good agreement with the expected porosities. The 3D reconstructions were done by importing the binary 2D image stacks into the software ORS Visual (Object Research Systems (ORS), Montreal, Canada). Figure 19a-c shows SEM mid-angle BSE image stacks of three samples with different porosities, and Figure 19d-f shows the corresponding 3D reconstructions of the porous network in white.

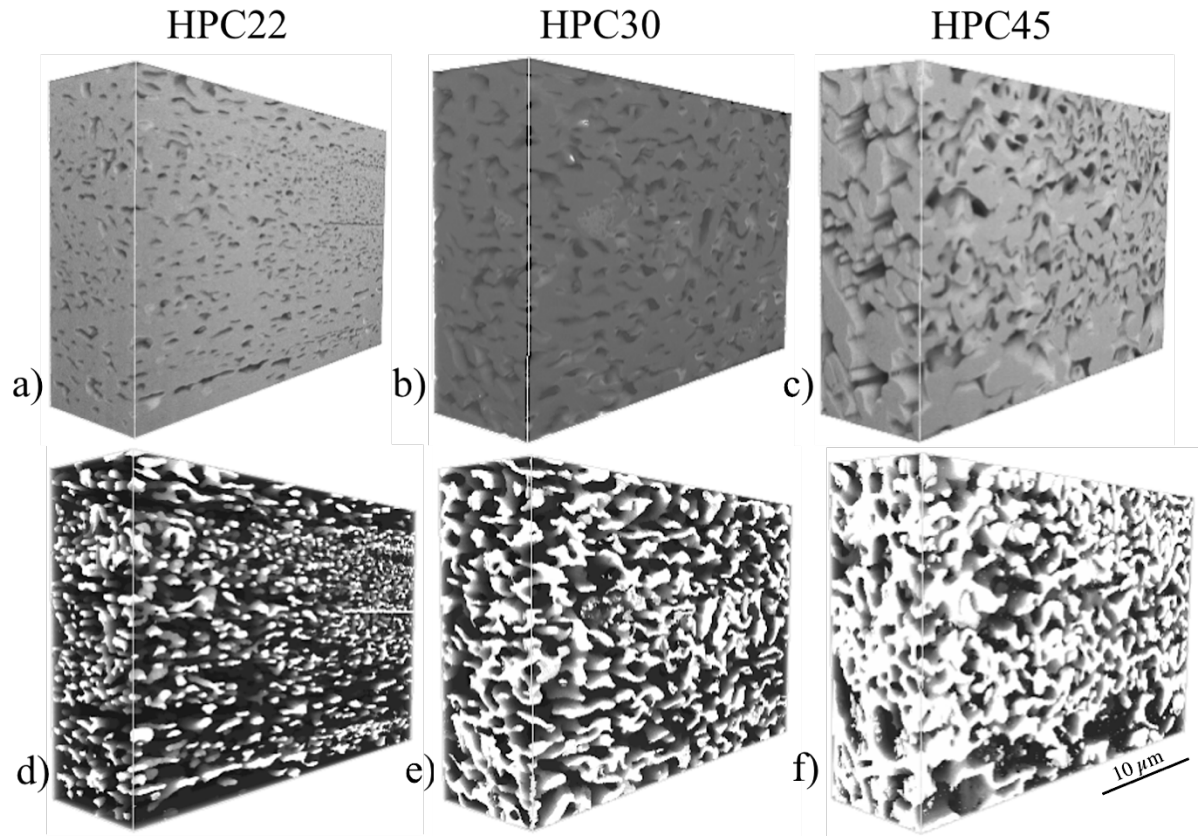

Figure 19. FIB-SEM mid-angle BSE image data sets (top) and 3D reconstructions of porous networks (bottom). The three samples are a,d) HPC22, b,e) HPC30 and c,f) HPC45.

5.2.3 Polymer film coatings

High spatial resolution 3D data on polymer film coatings on pellets were successfully obtained using FIB-SEM tomography. Before the start of the slice-and-image procedure, the pellets were coated with a few nanometre of palladium using a sputter. The ion-beam parameters used for the serial sectioning were 1 nA and 30 kV, the slice thickness was 30 nm and the total depth (z) was 5,5 µm. The electron-beam parameters used for imaging the cross-section surface were 1 kV and 10 pA and the cross section surface was imaged utilising a mid-angle BSE detector with scan speed 100 µs/pixel and 30 nm pixel size. Due to drift challenges, the data was acquired in sub-sequential steps, 30 images were acquired followed by a restart of the slice-and-image procedure. The sequential 2D images were aligned and cropped. The 3D reconstructions were done by importing the 2D image stacks into the software Dragonfly (Object Research Systems, Montreal, Canada). Figures 20-23 shows 3D reconstructions of mid-angle BSE SEM image stacks for four polymer film coatings.

Figure 20a, shows the full volume of the 3D reconstruction of the HPC25 polymer film coating on big core (666 μm) while Figure 20b shows further into the volume and Figure 20c even further. Regions with different porosities are marked in Figure 20c. Alternating less porous (yellow) and more porous regions (green) are marked in Figure 20c. These porous regions remain the same throughout the full reconstructed volume. The white parts at the top right of the volume is a residue from the protective platinum layer. In addition, it can be seen that the polymer film coating had detached from the core, hence the dark contrast below the coating.

The alternation of less porous and more porous regions in the HPC25 polymer film coating on the big core in Figure 20 can also be seen in the 3D reconstruction of the HPC40 polymer film coating on the big core in Figure 21. In addition to the alternation of the different porous regions, an air bubble is visualised in Figure 21a. As the HPC25 coating, the HPC40 coating had detached from the core, hence the dark contrast below the coating. The air bubbles are formed during the manufacturing of the pellets and are present in the coatings even before HPC is leached out.

The 3D reconstruction of the HPC40 polymer film coating on a small core (270 μm) in Figure 22 reveals an alternation between porous region (green) and solid region (blue). The solid regions are narrow compared to the porous regions. It is also observed that the different regions remains the same throughout the full reconstructed volume, see Figure 22a-c. The coating is still attached to the core, which is marked in Figure 22a.

In Figure 23, the 3D reconstruction of the HPC25 polymer film coating on small core is visualised. As the HPC40 coating on a small core, the HPC25 coating is still attached to the core. Here, the solid regions are larger than the porous regions, which is shown in Figure 23a. In addition, an air bubble is revealed in the middle of the volume, see Figure 23b. One can also see a channel, a feature that is unique for the HPC25 polymer film coating on small core. Further into the volume, Figure 23c, the channel has disappeared and only the alternation between porous and solid regions is present.

The polymer film coatings on big cores contain regions that are either less porous or more porous while the coatings on small cores contain regions that are either solid or porous. The fraction of solid regions appears to increase with decreasing amount of HPC and decreasing core diameter.

The channel appearing in the HPC25 polymer film coating on the small core in Figure 23b was further investigated by reconstructing a 3D volume from another HPC25 polymer film coating on a small core, see Figure 24. The full volume of the 3D reconstruction is visualised in Figure 24a and the interface between the coating and the core is highlighted with a white line. Figure

24a reveals a porous region at the interface between the coating and the core while the rest of the coating consists of a solid region. The SEM BSE image stack in Figure24a was segmented and the porous regions was extracted and visualised in red in Figure 24b. Further into the reconstructed volume, a channel appears and connects the top surface of the coating with the porous regions, see the red colour in Figure 24c. The presence of channels explains how the HPC could be leached out closest to the core at these solid regions. It is believed that the porous regions are formed by phase separation of EC and HPC during the drying of the polymer film coatings and that the solid regions contain entrapped droplets or regions of HPC that are not connected to the porous network (Marucci, *et al*., 2013; Andersson, *et al*., 2018). It should be noted that the pores visualised in the 3D reconstructions were, prior to leaching, occupied by HPC since non-leached films are completely solid. Similar channels may be micro-cracks observed in previous work where the micro-cracks were created in the coating caused by the build-up of hydrostatic pressure inside the pellet. (Marucci, *et al*., 2010

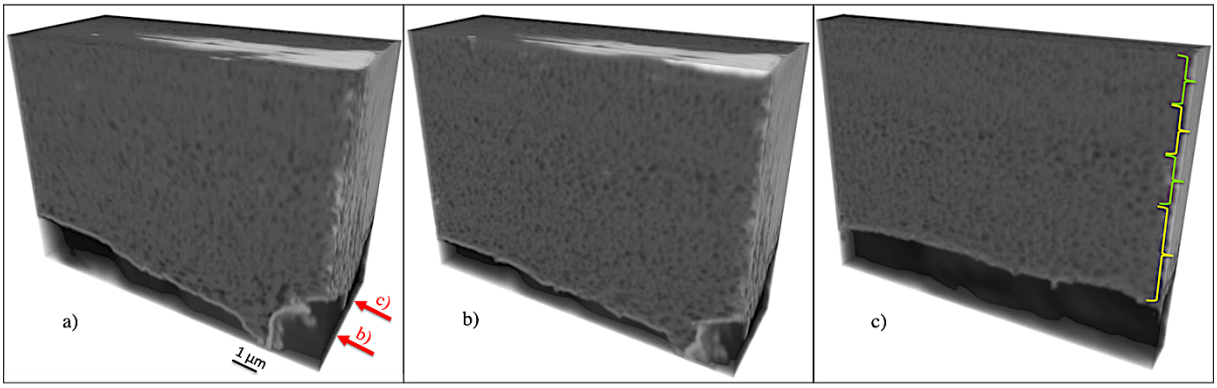

Figure 20. 3D reconstruction of a big pellet where a big core is coated with a HPC25 coating and where a) shows the full 3D volume and the red arrows mark where the volumes for b) and c) start, respectively. The internal structure of the coating looks similar throughout the full 3D reconstructed volume. Different porous regions are indicated with yellow (less porous) and green (more porous) to the right in c).

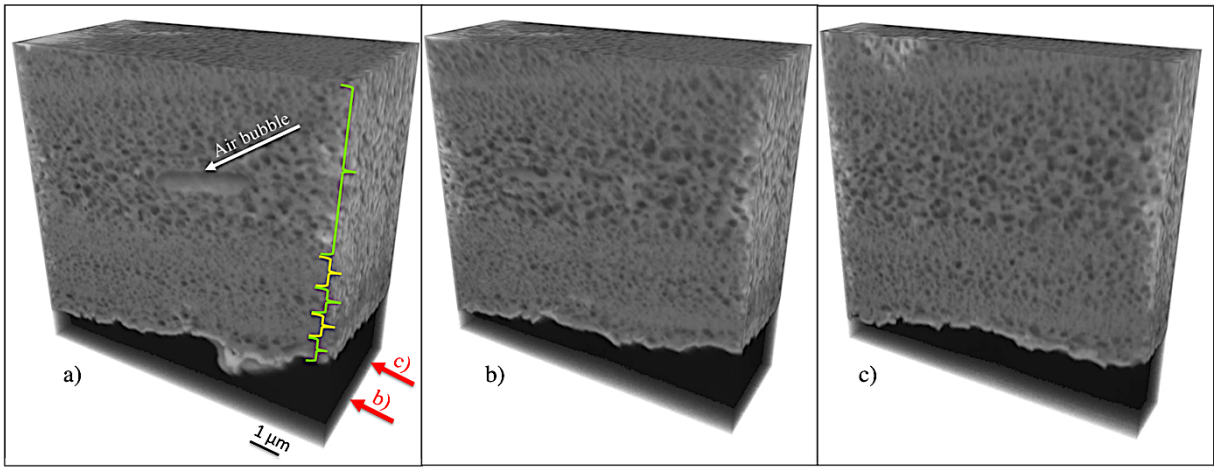

Figure 21. A 3D reconstruction of a big pellet where a big core is coated with a HPC40 coating and where a) shows the full 3D volume and the red arrows mark where the volumes for b) and c) start, respectively. Different porous regions are indicated with yellow (less porous) and green (more porous) in a). An air bubble is marked with a white arrow in a).

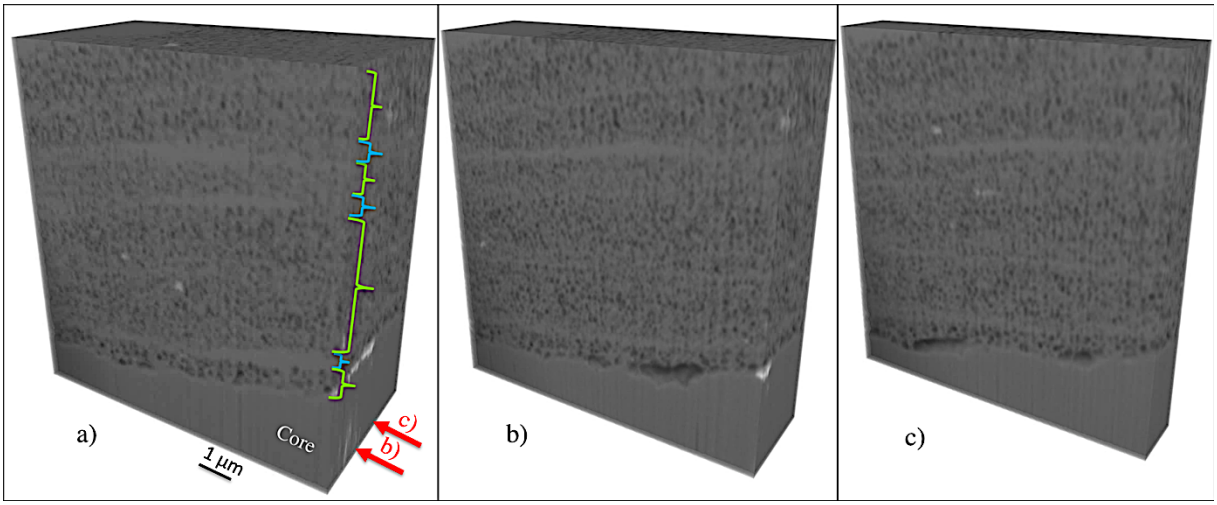

Figure 22. A 3D reconstruction of a small pellet where a small core is coated with a HPC40 coating and where a) shows the full 3D volume and the red arrows mark where the volumes for b) and c) start, respectively. In a) porous regions are marked in green and solid regions are marked in blue.

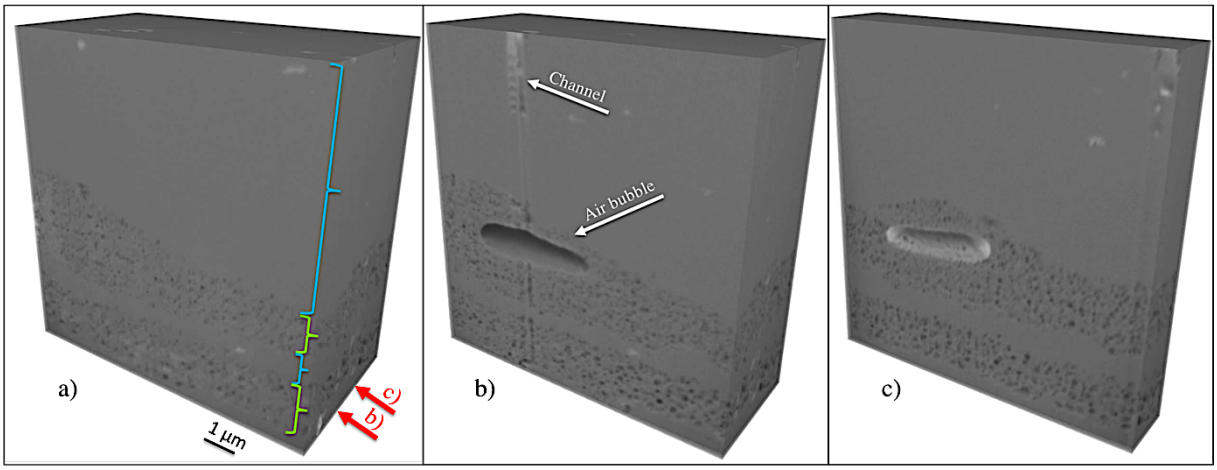

Figure 23. A 3D reconstruction of a small pellet where a small core is coated with a HPC25 coating and where a) shows the full 3D volume and the red arrows mark where the volumes for b) and c) start, respectively. In a) two porous regions are marked in green and two solid regions are marked in blue. Additional information is revealed further into the volume where b) shows an air bubble and a channel starting from the top marked with white arrows.

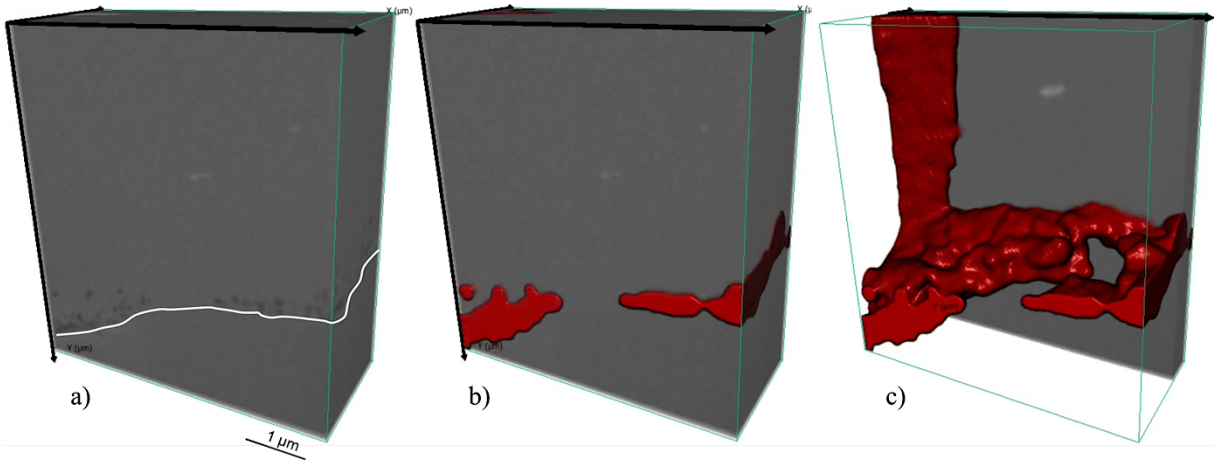

Figure 24. A 3D reconstruction of a small pellet where a small core is coated with a HPC25 coating and where a) shows the BSE SEM image stacks. The interface between the coating and the core is marked with a white line, b)shows the porous regions in red and c) reveals a channel connected to the porous regions.

5.3 Correlating internal structure of coatings with HPC release measurements

In order to understand the release properties of pellets, we correlated the internal structure of polymer film coatings with HPC release measurements in Paper VI. An overview of the eight pellets that were investigated can be seen in Figure 25. The manufacturing parameters for each pellet are presented in Table 2 in Section 3.2.2. The top row in Figure 25 shows the small (270 μm) pellets and the bottom row shows the big (666 μm) pellets. The internal structure of the coatings was revealed by performing cross sections utilising a focused ion beam and by imaging the cross section surfaces utilising a scanning electron microscope, which is illustrated in Figure 26.

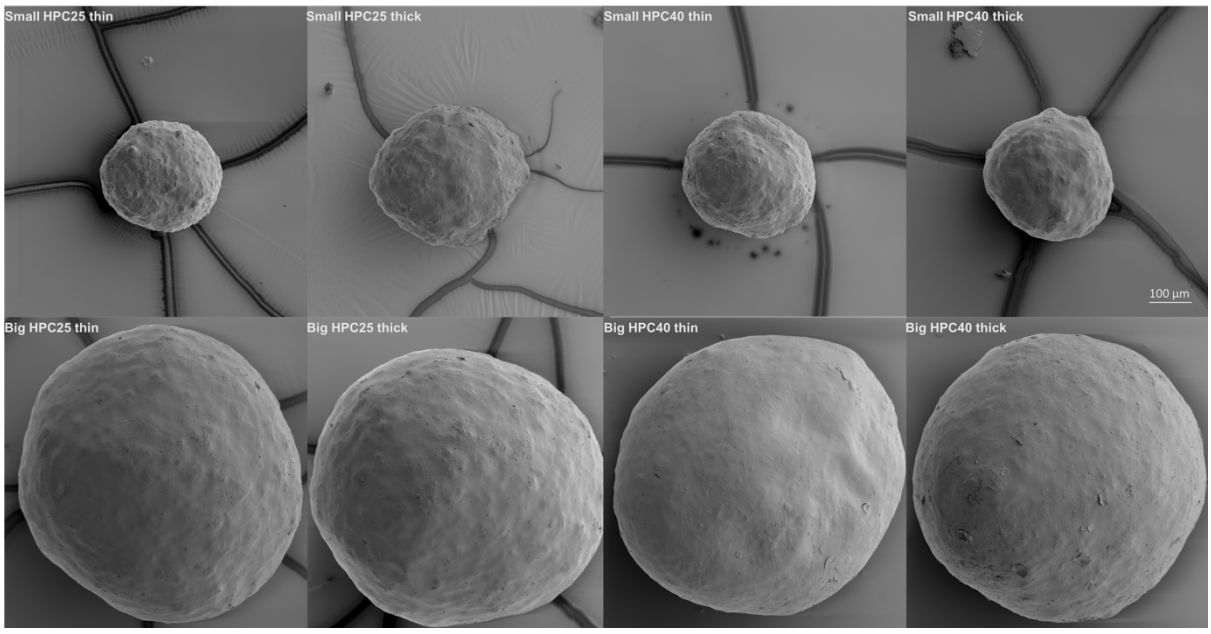

Figure 25. SEM BSE images of eight pellets manufactured with the different parameters: small (270 μm) or big (666 μm) core, ratio EC:HPC either 25:75 (denoted HPC25) or 40:60 (denoted HPC40), and thin (10 μm) or thick (40 μm) coating. The top row shows the small pellets and the bottom row shows the big pellets.

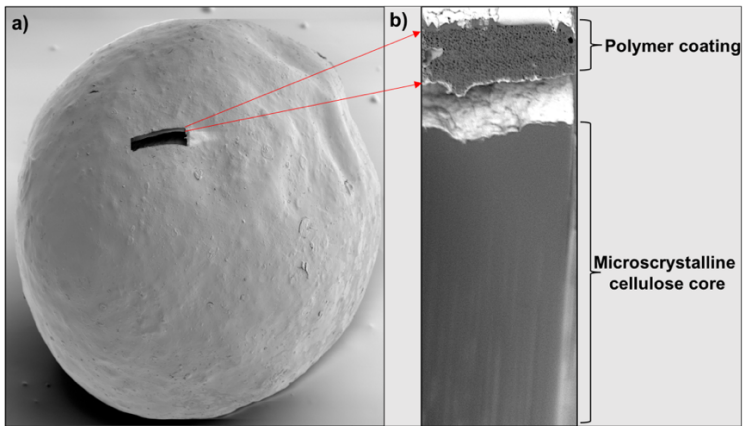

Figure 26. SEM images where a) shows a cross section on a pellet and b) shows a cross section surface of a polymer film coating and where the microcrystalline core and polymer coating are marked on the right.

The internal structure of each polymer film coating is seen in Figure 27. The interface between the coating and the core is marked with a white line in the cross sectional images. A common feature in all images is that different regions can be observed. Some of the porous regions have smaller pores while some regions have bigger pores. In addition, non-porous, solid, regions can be observed in some of the cross sections. The solid regions are more frequent in the HPC25 coatings, especially in the HPC25 coatings on small cores, than in the other coatings. Although not evident in Figure 27, the porous region below the solid region must be connected to the surface of the pellet for the HPC to be able to leach out. The leaching of the porous regions below the solid region could possibly be explained by the presence of channels (for example, see Figure 24c) further into the coating.

In contrast to the cross-sectional images which show the internal structure of one pellet, the data from the HPC release measurements give the average HPC release measured from many pellets. It should be noted that several pellets were studied using FIB-SEM images to ensure that the FIB-SEM were representative for the different types of film coatings. Figure 28 shows the HPC release from the pellets. The release of HPC is not complete for any of the pellets and it is decreasing with decreasing HPC content in the film. For the small core with thick HPC25 coating, only 68% HPC is released, thus 32% of the HPC is entrapped in the coating while the HPC release for the big core with thick HPC25 coating is 79%, meaning that only 21% HPC is entrapped. It has been shown for EC/HPC films (Marucci, *et al.*, 2013; Andersson, *et al.*, 2018) that a minimum amount of HPC around 20-22% is needed for the porous structure to form. It appears as using HPC concentrations close to the threshold value generate a greater share of solid regions (more entrapped HPC), hence resulting in a lower release rate. In addition, given

the same fraction of HPC and coating thickness, the release from small pellets is slower than the release from big pellets. The slower release rate for the small pellets can only be explained by an increase in tortuosity in these coatings. As the HPC25 coatings, the HPC40 coatings have lower release rates for the coatings on small pellets than the coatings on big pellets. Thus, the fraction of solid regions appears to increase with decreasing amount of HPC and with decreasing core diameter.

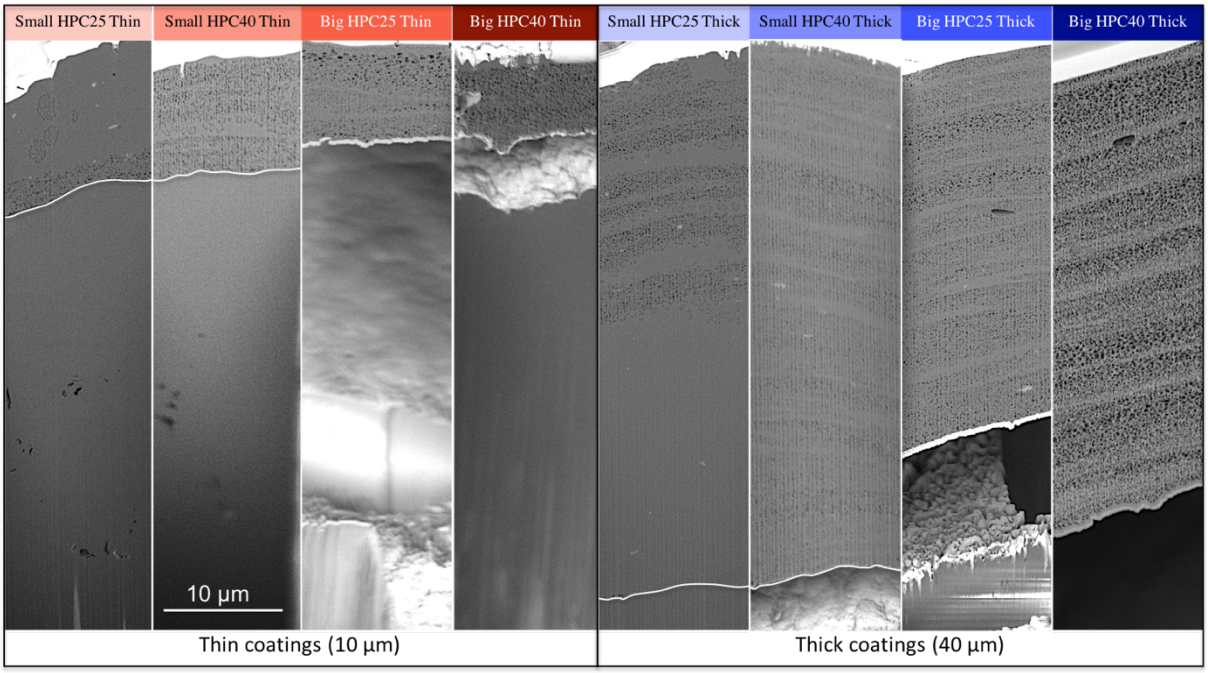

Figure 27. SEM BSE cross sectional images of pellets where thin coatings (10 μm) are seen on the left and thick coatings (40 μm) on the right.

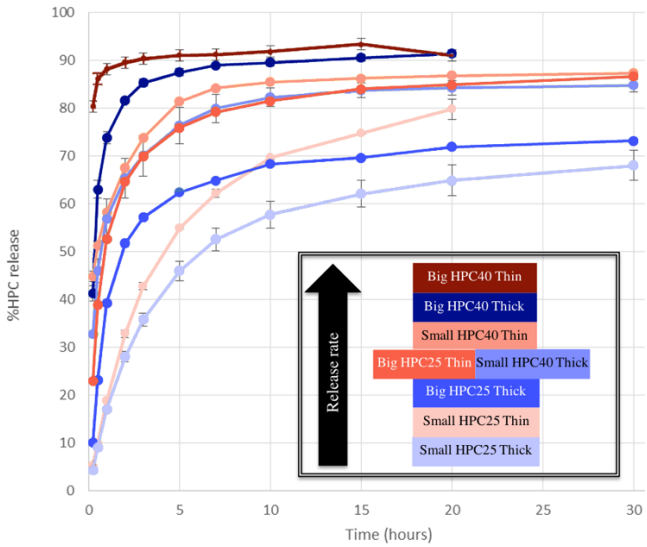

Figure 28. HPC-LF release curves of EC/HPC coated microcrystalline cores. The box to the bottom right shows the release rate increasing from the bottom to the top for all pellets. The colour code is the same as used in Figure 27.

5.4 Quantified characterisation of porous networks

Porous networks in model polymer films have been characterised and quantified by determining the pore morphology, pore size distribution, interconnectivity and tortuosity in Paper III and Paper IV.

5.4.1 Pore morphology and pore size distribution

The pore morphology and the pore size distribution of the porous structure in three model polymer films were characterised and quantified by fitting the largest spheres (sphere-pore size), maximal circles (maximal-circle-pore size) and maximal lines (maximal line-pore size) into the porous structure. Table 3 shows the values for each film. The sphere-pore sizes are smaller than the maximal circle-pore size which in turn are smaller than the maximal line-pore sizes which indicates that the pore morphology are flat and elongated, not spherical.

The total pore volume and median pore diameter for the three films were calculated to be 20 % and 0.35 μm for HPC22, 30 % and 0.60 μm for HPC30 and finally 44 % and 0.72 μm for HPC45. The spherical pore size distribution of the three films can be seen in Figure 29. It can be seen from Table 3 that sphere-pore size, maximal circle-pore sizes as well as the maximal line-pore sizes increases when going from the HPC22 film (least porous) to HPC30 (intermediate porous) and HPC45 (most porous). Consequently, the sphere-, maximal circle- and maximal line-pore sizes increases with increased porosity in the films. Line-pore sizes and circle-sphere sizes in different directions were also computed, see Paper IV for more details.

Table 3. Three pore shape measures where the values for sphere-pore size, circle-pore size and line-pore size for the three different model films.

Sample	HPC22	HPC30	HPC45
Sphere-pore size mean (min, max) [μm]	0.35 (0.05, 0.95)	0.60 (0.05, 1.55)	0.72 (0.05, 2.15)
Maximal circle-pore size mean (min, max) [μm]	0.62 (0.05, 2.95)	1.00 (0.05, 2.55.)	1.18 (0.05, 3.15)
Maximal line-pore size mean (min, max) [μm]	1.42 (0.05, 11.95)	2.57 (0.05, 8.55)	3.39 (0.05, 11.75)

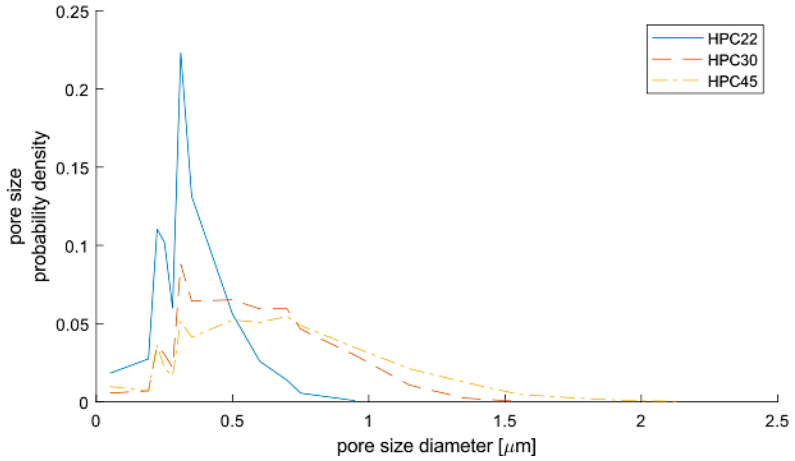

Figure 29. Spherical pore size distribution for three polymer films with different porosities. The spherical pore size distribution for HPC22 (blue line) has a peak around the median pore size 0.35 μm, whereas for HPC30 (red line) at 0.60 μm and for HPC45 (yellow) at 0.72 μm.

5.4.2 Quantification of interconnectivity

The interconnectivity in the model polymer films was quantified by using geodesic paths which are described in section 4.3.2.1. Geodesic paths are used to visualise individual through paths in 3D while geodesic tortuosity and geodesic channel strength are used to quantify the interconnectivity.

5.4.2.1 Individual through paths

Geodesic paths were computed for the three films HPC22, HPC30 and HPC45 with different porosities. A geodesic path is the shortest possible path from the top to the bottom of the porous network and a more detailed description of geodesic paths is described in the previous Section 4.3.2.1. The shortest geodesic path in each of the EC/HPC films is visualised in Figure 30. The figure also shows one geodesic path from the intermediate category and one from the long category. The structure of the paths in the cross-sectional plane can be seen in the front views (left column) while the side views show the paths' structure in the depth of the imaged volume (right column). The tortuosity values, i.e. the lengths of the paths through the porous networks, for each film are summarised in Table 4.

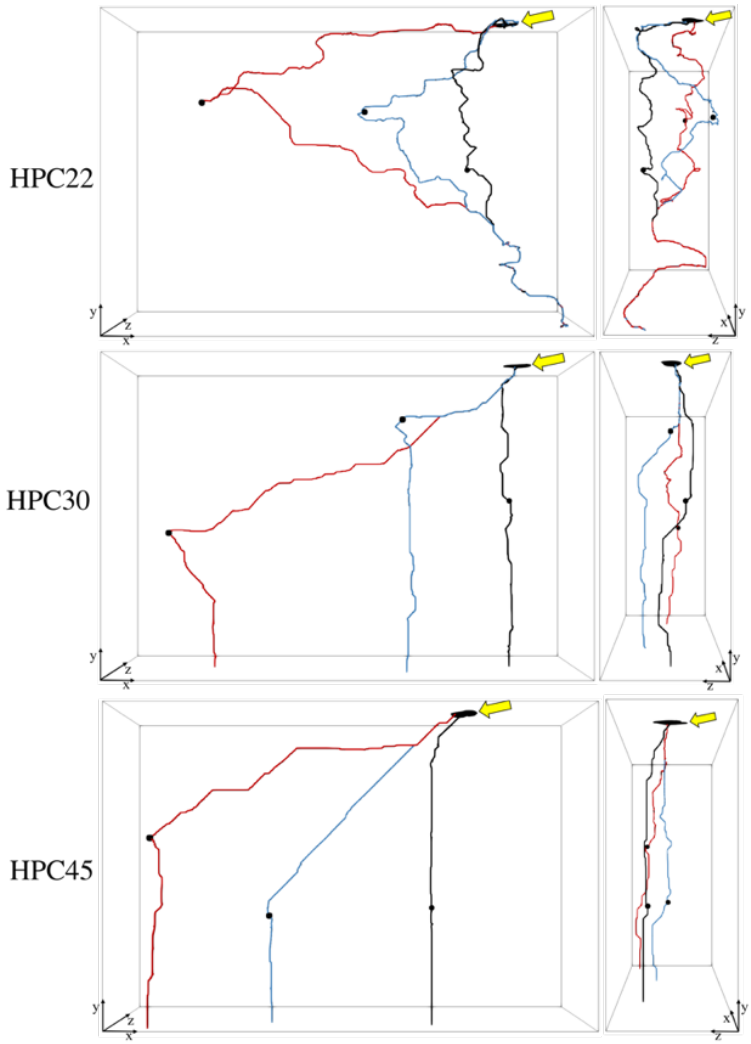

Figure 30. 3D visualisation of the shortest (black), an intermediate (blue) and a long (red) geodesic path, GeoPath(p), with the points p shown as black spheres. The images on the left show the cross sectional surfaces and the images on the right show the paths form the side. The inlets, where the paths have to start, are marked in black and indicated by yellow arrows. The outlet, where the paths have to end, is at the bottom plane.

Table 4. Tortuosity (relative geodesic path lengths) for leached EC/HPC films.

Film	HPC22	HPC30	HPC45
Shortest geodesic path tortuosity	2.37	1.16	1.07
Intermediate geodesic path tortuosity	2.93	1.44	1.35
Long geodesic path tortuosity	3.83	2.01	1.84

The polymer film with the lowest porosity (HPC22) shows a different path structure than the other two. The shortest geodesic path in HPC22 is more than twice as long as the shortest geodesic paths found in HPC30 and HPC45, see Table 4. This is explained by the shortest geodesic path in HPC22 being much more tortuous than the shortest paths in the other films. The shortest geodesic paths in HPC30 and HPC45 have similar path structures but the tortuosity values differ. It is observed that higher weight percentage of HPC in the film results in less tortuous paths and lower tortuosity values.

For the intermediate and long geodesic paths, the path structure of HPC22 is again different from those of HPC30 and HPC45. In the higher porosity films, the intermediate and long geodesic paths passing through the point (marked with a black sphere) that defines the geodesic path are relatively straight. In contrast, the intermediate and longest geodesic paths of HPC22 take long detours and share a large portion of their paths towards the bottom of the film with the shortest geodesic path. This can be related to the percolation onset around 22 wt % HPC discovered on these types of model polymer films (Marucci, *et al*., 2009).

5.4.2.2 Limiting layer

In order to capture parts of the porous network where paths coincide, quantification of channels has been done. If a channel has high channel strength, many paths pass through this channel, see Figure 31. There seems to be a limiting layer in the lower part in the HPC22 film where there are only two main channels, see yellow shaded area in Figure 31a. The quantitative information in Figure 31 for HPC22 indicates that the channel on the right is much more prominent than the channel on the left. 97% of the paths, i.e. over 9700 of the total 10 000 computed paths, pass through the channel on the right and the rest of the computed paths pass through the channel on the left. The same two channels are obtained independent of which pore at the top is chosen as inlet. In contrast, the prominent channels in HPC30 and HPC45 depend on the chosen inlet pore.

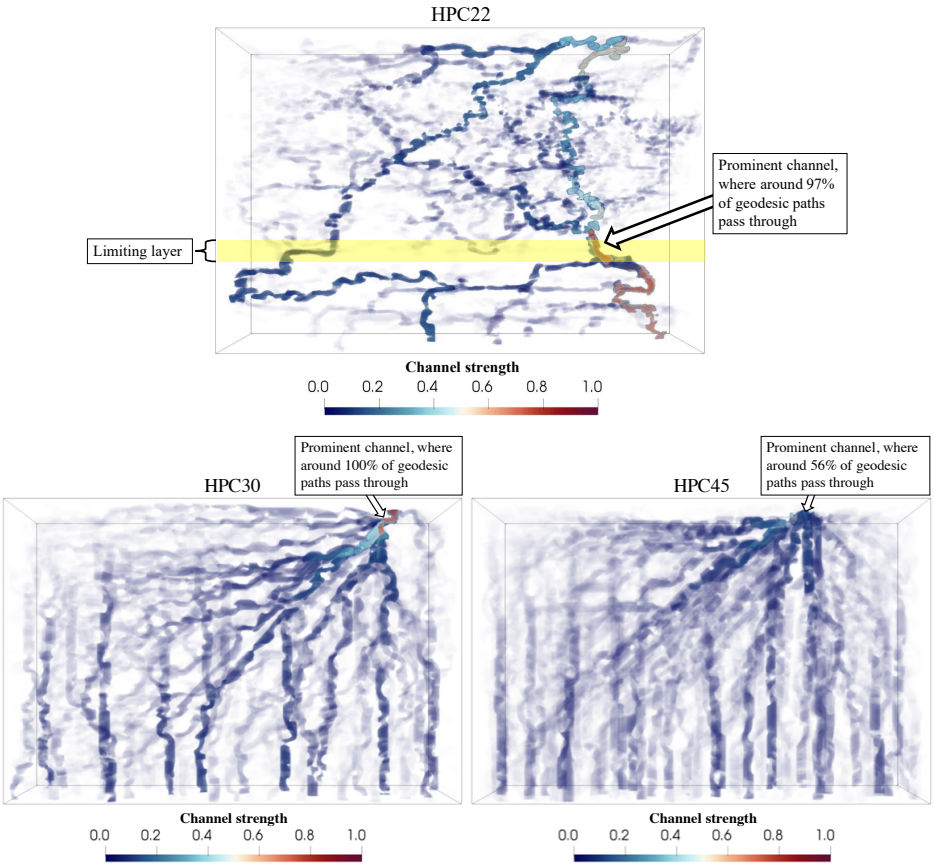

Figure 31. 3D visualisation of geodesic channel strength for HPC22, HPC30 and HPC45 model polymer films. In the colour scale, the same for all three images, red corresponds to high channel strength and blue to low channel strength. The opacity is low for channels of low channel strength. In HPC22, a limiting layer is marked with a yellow shaded area.

5.4.2.3 Tortuosity

The directional tortuosity for the full porous networks for the three different films, HPC22, HPC30 and HPC45, give information about the lengths of the paths in different directions. The tortuosity values for the three films are shown in Table 5. The tortuosity is visualised in Figure 32 for HPC22, HPC30 and HPC45, in the y-direction (top row) and in the x-direction (bottom row). The tortuosity values for HPC22 are considerably larger than the values for the other two films, both in the x-direction (τ_x) and y-direction (τ_y). Regarding the tortuosity in the y-direction for HPC22, the left half of the film has high tortuosity, values above three, while the right half of the film has lower tortuosity with values around 2. The tortuosity values for HPC30 and HPC45 are quite similar. One explanation for the higher tortuosity for HPC22 compared to HPC30 and HPC45 can be that HPC22 is close to the percolation onset while HPC30 and HPC45 are high above it (Marucci, *et.al.*, 2013).

Table 5. Tortuosity values in direction x (τ_x) and y (τ_y) for the full porous networks in the model polymer films HPC22, HPC30 and HPC45.

Film	HPC22	HPC30	HPC45
τ_x (min, max)	1.27 (1.11, 2.17)	1.10 (1.06, 1.43)	1.08 (1.04, 1.38)
τ_y (min, max)	2.75 (2.07, 4.62)	1.19 (1.10, 1.55)	1.10 (1.04, 1.55)

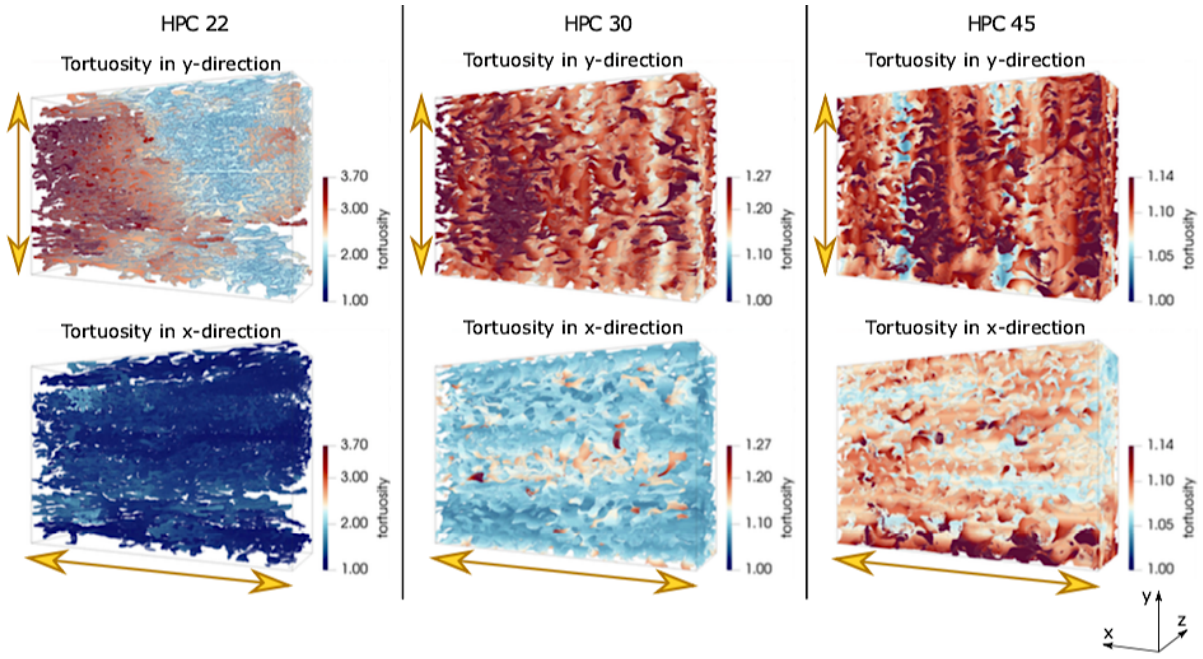

Figure 32. Tortuosity for HPC22 (left), HPC30 (middle) and HPC45 (right), computed in the y-direction (top row) and in the x-direction (bottom row). The directions are indicated by yellow arrows.

5.5 Mass transport

In order to correlate the porous network in model polymer films with mass transport properties, the effective diffusion coefficient was both simulated and experimentally measured in Paper V.

5.5.1 Simulated diffusion

The simulated diffusion through the model polymer films with different porosities is shown in Figure 33a-c, where one single line on the top in the middle of the volume has been selected to visualise the flux lines from top to bottom. The colours of the flux lines are correlated to the magnitude of the flux. The blue colour corresponds to low flux while red colour corresponds to higher flux. Bottlenecks, i.e. tight pores that limits the mass transport, can be identified within the porous network due to the strong red flux lines. The diffusion through the film with lowest porosity, HPC22, was simulated in 5 separate layers that were overlapping with the neighbouring layers, and the top sub-volume is visualised in Figure 33a. Regarding HPC30 and HPC45, flux lines that originates from one line at the top are shown in Figure 33b-c. In the film with intermediate porosity, HPC30 in Figure 33b, two main channels are responsible for the diffusion. The diffusion paths in the film with highest porosity, HPC45 in Figure 33c, are evenly distributed throughout the porous structure which can be seen by the flux lines being evenly distributed along the line at the top of the volume. However, it should be mentioned that depending on where the top line from where the flux lines are visualised, the flux lines might vary within the volume. HPC45 may have a more evenly distributed mass transport through the volume than HPC30 and HPC22 since HPC45 is further away from the percolation onset and thus has the highest porosity and the most well-connected pore structure among all the model polymer films. The simulated effective diffusion coefficients (simulated D_{eff}) for the films are shown in Table 6. The simulated D_{eff} for HPC22 was very low compared to the values for HPC30 and HPC45. The low simulated D_{eff} for HPC22 stems most likely from the very tortuous porous structure controlling the diffusion, seen in section 5.4.2.3. The HPC30 film had lower simulated D_{eff} than the HPC45 film, resulting mainly due to an increased tortuosity.

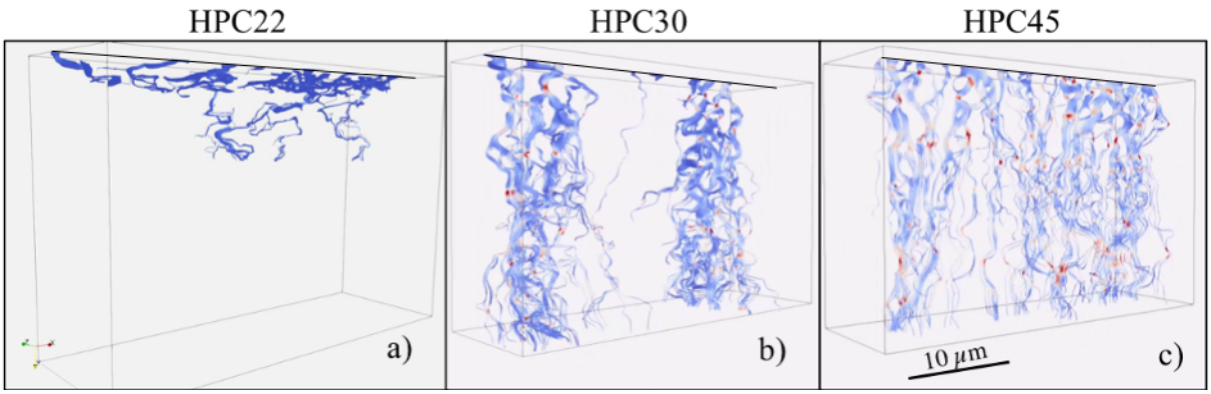

Figure 33. The 3D simulated diffusion is shown for the different model polymer films a) HPC22, b) HPC30 and c) HPC45. The red color corresponds to higher flux values and the blue color to lower flux values. In a) the diffusion is simulated in separate layers due to the large internal variation in the porous structure, diffusion in the top sub-volume is shown. In b) and c) one single line at the top and its flux lines are shown. For b) HPC30 two main channels can be seen and for d) HPC45 the flux lines are evenly distributed throughout the volume.

5.5.2 Experimentally measured diffusion

The effective diffusion coefficient was calculated from the permeability measurements using a diffusion cell. The calculated effective diffusion coefficients (Experimental D_{eff}) are presented in Table 6. The experimental D_{eff} for HPC22 was very low in comparison to the values for HPC30 and HPC45, which is in agreement with the outcome from the simulated D_{eff} values.

Table 6. The simulated and experimentally measured effective diffusion coefficients for HPC22, HPC30 and HPC45.

HPC [wt %]	Simulated D_{eff} [10^{-12} m^2/s]	Experimental D_{eff} [10^{-12} m^2/s]
22	6,25	7,52
30	203	270
45	518	637

By comparing the simulated and experimentally measured D_{eff} it can be seen that the simulated data in all three cases are lower than the experimentally measured D_{eff}. The underestimation is of the order of 15 to 25%. The differences are likely to depend mainly on the fact that only a small part of the film was imaged and used for simulations, while experimental diffusion measurements were made on the entire film. The simulated and experimentally measured D_{eff} correspond well to each other while a previous study showed a difference of more than 300% (Gebäck, *et al*., 2015). This shows that the method of using experimental FIB-SEM data in combination with diffusion simulations is a powerful approach to use when studying the correlation between materials structures and properties.

Chapter 6
Conclusions

In order to image the internal structure of soft, porous and poorly conductive materials with high spatial resolution in 2D and 3D, FIB-SEM is a powerful technique to utilise. Our aim of this work has been to reveal the internal structure of soft, porous and poorly conductive materials to be able to correlate materials structures with materials properties. However, for porous and poorly conductive materials, acquisition of FIB-SEM tomography data remains challenging. The problems are charging and damage induced by the ion and electron beams as well as the low contrast in images of soft materials. It should be noted that even though different effects have been illustrated many times previously they have not been collected and described jointly but instead been reported separately in several different papers.

In our work we have collected all relevant effects and techniques for soft, porous and poorly conductive materials and also further developed the method for this category of materials. Our ambition has been to develop an approach that is time efficient and does not suffer from artefacts of staining and freezing. We would like to emphasise that our approach, presented in this work, combines a minimal and gentle sample preparation prior to the FIB-SEM work and an optimisation and further development of FIB-SEM parameters for porous materials. A self-learning segmentation algorithm was developed to address the segmentation challenge that pores introduce for quantitative evaluation of FIB-SEM tomography data.

We demonstrated our protocol on a model system for polymer film coatings used for controlled drug release. 3D reconstructions of three types of polymer films with different porosities were successfully obtained and segmented. The model polymer films are based on two polymers, ethyl cellulose (EC, water insoluble) and hydroxypropyl cellulose (HPC, water soluble). Upon contact with water, the HPC leaches out leaving a porous EC film coating where the porous network acts as transport paths for the drug. In order to understand what gives rise to the transport properties of the material, the correlation between the materials structures and materials properties is crucial. The materials structures have been identified by quantitative characterisation of the porous networks, and the materials properties have been identified by both simulated and experimentally measured diffusion.

The quantified characterisation of the porous networks showed that the model polymer film with least amount of added HPC, HPC22 with 22 wt% HPC, had the longest and most tortuous

paths, smallest pore size as well as most anisotropic pore morphology compared to the other two films with higher amount of added HPC, HPC30 and HPC45. This structural information could explain the significantly lower simulated and experimentally measured effective diffusion coefficients in the HPC22 film in comparison to the other two films. The materials structures, such as pore morphology and pore size distribution are important parameters and for quantitatively describe the functional microstructure of the porous materials. In addition, the 3D tomography data provide important insights in pore interconnectivity. Developing the mathematical treatment of the experimental 3D data led to the identification and quantification of tortuosity and geodesic paths that are very useful characterisation measures for understanding what controls the transport properties through porous materials.

The protocol for optimisation of FIB-SEM parameters enabled the study of internal structure of pellets which have a more challenging morphology. The pellet morphology is representative for the medical application of these polymer films. The optimised FIB-SEM parameters were utilised to image cross section surfaces as well as performing 3D reconstructions of the internal structures of polymer film coatings coated on pellet cores. The cross sectional images showed that there exist different characteristic regions such as solid, less porous and more porous regions in the polymer film coatings. The 3D reconstructions of thin coatings revealed channels connecting the porous regions to the top surface of the pellets through solid regions which explains the release of HPC through solid regions. The cross sectional images was linked with experimentally measured HPC release rates which showed that the fraction of solid regions appears to increase with decreasing amount of HPC as well as decreasing core diameter.

Chapter 7
Outlook

Correlating materials structures to properties for soft, porous and poorly conducting materials utilising quantitative 3D reconstruction by FIB-SEM tomography is a powerful technology. The here developed protocol for optimisation of FIB-SEM parameters is applicable to a wide range of materials and could provide new valuable insights by its quantitative high spatial resolution 3D visualisation. However, the acquisition of FIB-SEM tomography data on soft, porous and poorly conductive materials is relatively time consuming as a semi-automatic approach. One way to make this a fully automatic approach, i.e. more time efficient, incorporation of automatic carbon gas injection prior to imaging of the cross section surface into the software would be truly beneficial. The automatic acquisition of FIB-SEM tomography data would make it easier and more convenient to further investigate pellets having thick coatings. It would be important to reveal if the different regions present in the thin coatings are also present in the thick coatings on pellets.

Another aspect that would be very interesting to further study is the contrast mechanism between the EC and HPC. Our work indicates that the leaching of HPC may change the structure of the continuous EC network in the polymer films. A comparison between unleached and leached films would provide valuable information about the formation of the porous network during leaching. At present the low contrast between EC and HPC has not allowed these studies. A further exploration of the different signals, e.g. mix between signals from the BSE and SE detectors, that can be extracted from the films during studies in the FIB-SEM could provide a method sufficiently enhanced difference in signal from the two phases.

Another interesting method to apply on unleached films would be to change the pressure inside the chamber to allow the presence of water vapor, and thus leach out the HPC in-situ. It would also be interesting to make a cross section in a film containing both EC and HPC, leach out HPC ex-situ and then insert the film into FIB-SEM again and image the cross section surface. This could then lead to that a correlation of the images before and after leaching could reveal where HPC is entrapped in EC.

It would also be interesting to directly reveal the through paths through the porous network by exposing one side of the porous EC film into solution with marker molecules, containing e.g. metals that could be easily identified by contrast or energy dispersive x-ray spectroscopy, and

let the fluid be transported through the film. The film would be subsequently studied in the FIB-SEM and the marker molecules tracked in 3D tomography data.

Moreover, the porous network in pellets develops during manufacturing in a fluidised bed where polymer solution droplets are deposited on the pellet cores. A structural investigation of the polymer solution droplets would reveal important information about the development of the alternating less and more porous regions observed in the resulting polymer film coatings.

References

Andersson, R.U., Mobley, D., Lank, B., Saltzstein, D., Susset J. & Brown J.S. (1999). Once daily controlled versus immediate release oxybutynin chloride for urge urinary incontinence. *The Journal of UrologY*. 161(6), 1809-1812.

Andersson, H., Hjärtstam, J., Stading, M, Von Cosrwant, C. & Larsson, A. (2013). Effects of molecular weight on permeability and microstrucutre of mixed ethy-hydroxypropyl-cellulose films. *European Journal of Pharmaceutical Sciences*. 48, 240-248.

Andersson, H., Häbel, H., Olsson, A., Sandhagen, S., Von Corswant, C., Hjärtstam, J., Persson, M., Stading, M. & Larsson, A. (2016). The influence of the molecular weight of the water-souble polymer on phase-separated films for controlled release. *International Journal of Pharmacerutics*. 511, 223-235.

Andersson, H., Marucci, M., Andersson, Härddelin, L., Hjärtstam, J., Stading, M., Von Corswant, C. & Larsson, A. (2018). New insights in the influence of manufacturing conditions and molecular weight on phase-separated films intended for controlled release. *International Journal of Pharmaceutics*. 536, 261-271.

Armatas, G.S. (2006). Determination of the effects of the pore size distribution and pore connectivity on the pore tortuosity and diffusive transport in model porous networks. *Chemical Engineering Science*. 61, 4662-4675.

Barman, S., Rootzén. H. & Bolin, D. (2018). Prediction of Diffusive Transport Through Polymer Films from Characteristics of the Pore Geometry. *AIChE Journal*. 65, 446-457.

Bassim, N.D., De Gregorio, B.T., Kilcoyne, A.L.D., Scott, K., Chou, T., Wirick, S., Cody, G. & Stroud, R.M. (2011). Minimizing damage during FIB sample preparation of soft materials. *Journal of Microscopy*. 245, pp. 288-301.

Bassim, N., Scott. & Giannuzzi, L.A. (2014). Recent Advances in Focused Ion Beam Technology and Applications, *MRS Bull,* 39, pp. 317-325.Inkson, B.J., Mulvihill, M. & Möbus, G. 3D determination of grain shape in a FeAl-based nanocomposite by 3D FIB tomography. *Scripta Mater* 45. 753-758.

Berg, C.F. (2012) Re-examining Archie's law: Conductance description by tortuosity and constriction. Physical Review E: Statistical, Nonlinear, and Soft Matter Physics, 86(4)

Blayvas, I., Bruckstein, A. & Kimmel, R. (2006). Efficient computation of adaptive threshold surfaces for image binarization. *Pattern Recognition*. 39, 89-101.

Breiman, L. (2001). Random forests, *Machine learning* **45**, 5-32.

Brostow, W,. Gorman, BP, & Olea-Mejia, O. (2007). Focused ion beam milling and scanning electron microscopy characterization of polymer+metal hybrids *Materials Letters*. 61, 1333–1336

Cantoni, M. & Holzer, L. (2014). Advances in 3D Focused Ion Beam Tomography, *MRS Bull,* 354-360.

Deerinck, T.J., Bushong, E.A., Lev-Ram, V., Shu, X., Tsien, R.Y. & Ellisman, M.H. (2010). Enhancing serial block-face scanning electron microscopy to enable high resolution 3-D nanohistology of cells and tissues. *Microscopy and microanalysis*. 16(2), 1138-1139.

Deng, B,. Barki, KG,. Ghatak, S,. Roy S,. McComb, DW & Sen, CK. (2015*)*. FIB/SEM Tomography of Wound Biofilm. *Microscopy Microanalysis*. 21(Suppl 3), 205.

De Winter, D.A.M., Schneijdenberg, C.T.W.M., Lebbink, M.N., Lich, B.,Verkleij, A.J., Drury M. R. & Humbel, B.M. (2009). Tomography of Insulating Biological and Geological Mateirals Using Focused Ion Beam (FIB) Sectioning and Low-kV BSE Imaging. *Journal of Microscopy*. 233(3), 372-383.

Drobne, D., Milani, M., Leser, V. & Tatti, F. (2007). Surface Damage Induced by FIB Milling and Imaging of Biological Samples is Controllable. *Microscopy Research and Technique* 70, 895-903.

Dubochet, J., Adrian, M., Chang, J-J., Omo, J-C., Lepault, J., McDowall, A.W. & Schultz, P. (1988). Cryo-electron microscopy of vitrified samples. *Quarterly Review of Biophysics*. 21(2), 129-228.

Edsbäcker, S., Larsson, B.B., Larsson, P., Lundin, P., Nilsson, Å., Ulmius, J. & Wollmer, P. (2003). A pharmacoscintigraphic evaluation of oral budesonidegiven as controlled-release (Entocort) capsules. *Alimentary Pharmacology & Therapeutics*. 17(4), 525-536.

Efford, N. Digital image processing. (2000). New York: Addison Wesley.

Ferrero, C. & Jiménez-Castellanos, M.R. (2002). The influence of carbohydrate nature and drying methods on the compaction properties and pore structure of new methyl methacrylate copolymers. *International Journal of Pharmaceutics*. 248, 157-171.

Frohoff-Hülsmann, M.A., Schmitz, A. & Lippold, B.C. (1999). Aqueous ethyl cellulose dispersions containing plasticizers of different water solubility and hydroxypropyl methylcellulose as film material for diffusion pellets I. Drug release rates from coated pellets. *International Journal of Pharmaceutics*. 177, 69-82.

Gebäck, T., Marucci, M., Boissier, C., Arnehed, J. & Heintz, A. (2015). Investigation of the Effect of the Tortuous Pore Structure on Water Diffusion through a Polymer Film Using Lattice Boltzmann Simulations. *The journal of Physical Chemistry B*. 119, 5220-5227.

Gebäck, T. & Heintz, A. (2014). A Lattice Boltzmann Method for the Advection-Diffusion Equation with Neumann Boundary Conditions. *Commucations in Computational Physics*. 15(2), 487-505.

Ghanbarian, B., Hunt, A.G., Ewing, R.P. & Sahimi, M. (2013). Tortuosity in porous media: a critical review. *Soil Science Society of America Journal*, 5,1461–1477,

Ghassemzadeh, J. & Sahimi, M. (2004). Pore network simulation of fluid imbibition into paper during film: II. Characterization of paper's morphology and computation of its effective permeability tensor. *Chemical Engineering Science*. 59, 2265-2280.

Giannuzzi, L.A. & Stevie, F.A. (2005). *Introduction to focused ion beams*: Instrumentation, theory, techniques and practise. USA: Springer

Ginzburg, I. (2005). Equilibrium-Type and Link-Type Lattice Boltzmann Models for Generic Advection and Anisotropic-Dispersion Equation. *Adv. Water Resour*. 28, 1171–1195.

Goldstein, J., Newbury, D., Joy, D., Lyman, C., Echlin, P., Lifshin, E., Sawyer, L. & Michael, J. (2003). Scanning electron microscopy and x-ray microanalysis 3rd edition. (New York:Plenum)

Gruber, P., Longer, M.A. & Robinson, J.R. (1987). Some biological issues in oral, controlled drug delivery. *Advanced Drug Delivery Reviews*. 1(1), 1-18.

Harris, L.B., Moncrieff, D.A. & Robinson, V.N.E. (1976). High-resolution examination of uncoated insulators by SEM applied to grain boundaries in sodium chloride. *Physica Status Solidi*. 35, 371-377.

Hayles M.F., Stokes D.J., Phifer, D. & Findlay, K.C. (2007). A technique for improved focused ion beam milling of cryo-prepared life science samples, *Journal of Microscopy,* 226(3), 263–269.

Heymann, J.A., Hayles, M., Gestman, I., Giannuzzi, L.A., Lich B. & Subramaniam, S. (2006). Site-specific 3D imaging of cells and tissues with a dual beam, microscope. *Journal of Structural Biology*. 155, 63-73.

Holzer, L., Indutnyi, F., Gasser, P.H., Much, B. & Wegmann, M. (2004). Three-dimensional analysis of porous $BaTiO_3$ ceramics using FIB nanotomography. *Journal of Microscopy*. 216, 84-95.

Holzer, L., Weidenmann, D., Münch, B., Keller, L., Prestat, M., Gasser, P.H., Robertson, A. & Grobéty, B. (2013). The influence of constrictivity on the effective transport properties of porous layers in electrolysis and fuel cells. *Journal of Materials Science*, 48(7), 2934–2952.

Hutton, J.T. & Morris, J.L. (1992). Long-acting carbidopa-levodopa in the management of moderate and advanced Parkinson's disease. *Neurology*. 42(1), 51-56.

Inkson, B.J., Steer, T., Mobus, G. & Wagner, T. (2001). Subsurface nanoindentation deformation of Cu-Al multilayers mapped in 3D by foused ion beam microscopy. *Journal of Microscopy*. 201, 256-269.

Jansson, A., Nafari, A., Sanz-Velasco, A., Svensson, K., Gustafsson, S., Hermansson, A-H. & Olsson, E. (2013). Novel Method for Controlled Wetting of Materials In the Environmental Scanning Electron Microsope. *Microscopy and Microanalysis*. 19, 30-37.

Joergensen, P.S., Hansen, K.V., Larsen, R. & Bowen, J.R. (2010). A framework for atuomatic segmentation in three dimensions of microstructural tomography data. *Ultramicroscopy*. 110, 216-228.

Jones, R.A.L. & Richards, R.W. (1999). Polymers at surfaces and interfaces, Cambridge, Univeristy Press, Cambridge, UK.

Jones, A.C., Arns, C.H., Hutmacher, D.W., Milthorpe, B.K. & Sheppard, A.M.A. (2009) The correlation of pore morphology, interconnectivity and physical properties of 3D ceramic scaffolds with bone ingrowth. *Biomaterials*. 30, 1440–1451.

Julbe, A. & Ramsay, J.D.F. (1996). Methods for the characterisation of porous structure in membrane materials. In: Burggraaf, A.J, Cot, L. (EDS). Fundamentals of inorganic membrane science and technology. Elsevier Science. 67-118.

Kim. S., Park, MJ., Balsara, NP., Liu, G. & Minor, AM. (2011). Minimization of focused ion beam damage in nanostructured polymer thin films. *Ultramicroscopy*. 111, 191–199.

Kirk, E.C.G., Williamns, D.A. & Ahmed, H. (1987) In situ microsectioning and imaging of semiconducttor devices. *Insitute of Physics Conference Series*. 87, 691-696.

Kizilyaprak, C., Stierhof, Y.D. & Humbel, B.M. (2019). Volume microscopy in biology: FIB SEM tomography. *Tissue and Cell*. 57, 123-128.

Klein, E. (2002). The role of extended-release benzodiazepines in the treatment of anxiety: a risk-benefit evaluation with a focus on extended-release alprazolam. *The journal of clinical psychiatry*. 63(14), 27-33.

Krüger, T., Kusumaatmaja, H., Kuzmin, A., Shardt, O., Silva, G. & Viggen, E.M. (2017) The Lattice Boltzmann Method. *Springer International Publishing*. (DOI: 10.1007/978-3 319-44649-3)

Langer, R. & Peppas, N. (1983). Chemical and Physical Structure of Polymers as Carriers for Controlled Release of Bioactive Agents: A Review. *Macromolecular Science Part C*. 23(1), 61-126.

Lecomte, F., Siepmann, J., Walther, M., Macrae, R.J. & Bodmeir, R. (2003). Blends of Enteric and GIT-Insoluble Polymers Used for Film Coating: Physicochemical Characterization and Drug Release Patterns, *Journal of Controlled Release*. 89, 457-471.

Lindstedt, B., Ragnarsson, G. & Hjärtstam, J. 1989. Osmotic pumping as a release mechanism for membrane-coated drug formulations. *Int. J. Pharm. 56*, 261-268.

Markl, D., Strobel, A., Schlossnikl, R., Bøtker,J., Bawuah, P., Ridgway, C., Rantanen, J., Rades, T., Gane, P., Peiponen, K-E. & Zeitler, J.A. (2018). Characterization of pore structures of pharma- ceutical tablets: a review. International Journal of Pharmaceutics, 538:188–214.

Marucci, M., Hjärtstam, J., Ragnarsson, G., Iselau, F. & Axelsson, A. (2009). Coated Formulations: New Insights Into the Release Mechanism and Changes In the Film Properties with a Novel Release Cell. *Journal of Controlled Release*, 136(3), 206-212.

Marucci, M., Ragnarsson, G., Nilsson, B. & Axelsson, A. (2010). Osmotic pumping release from ethyl–hydroxypropyl–cellulose-coated pellets: A new mechanistic model. *Journal of Controlled Release*. 142, 53–60

Marucci, M., Arnehed, J., Jarke, A., Matic, H., Nicholas, M., Boissier, C. & Von Corswant, C. (2013). Effect of the Manufacturing Conditions On the Structure and Permeability of Polymer Films Intended for Coating Undergoing Phase Separation, *European Journal of Pharmaceutics and Biopharmaceutics*. 83, 301-306.

Mayer J, Giannuzzi LA, Kamino T & Michael J (2007). TEM Sample Preparation and FIB Induced Damage. *MRS Bulletin*.

Michael, R.J. (2011). Focused Ion Beam Induced Microstructural Alterations: Texture Development, Grain Growth, and Intermetallic Formation. *Microscopy and Microanalysis* 17, 386-397

Moghadam, S.H., Dinarvand, R., Cartilier, L.H. (2006). The focused ion beam technique: A useful tool for pharmaceutical characterization. *International Journal of Pharmaceutics*. 321, 50–55.

Moncrieff, D.A., Robinson, V.N.E. & Harris, L.B. (1978). Charge neutralisation of insulating surfaces in the SEM by gas ionisation. *Journal of Physics D: Applied Physics*. 11, 2315-2325.

Muschert, S., Siepmann, F., Leclercq, B., Carlin, B. & Siepmann, J. (2009). Prediction of drug release from ethylcellulose coated pellets. *Journal of Controlled Release*.135,71–85

Narayan, K. & Subramaniam, S. (2015). Focused Ion Beams in Biology. *Nature Methods*. 12, 1021-1031

Nastasi, M., Mayer, J.W. & Hirvonen, J.K. (1996). Ion-solid interactions: Fundamentals and applications. Cambridge University Press, Great Britain.

Norton, I.T. & Frith. W.J. (2001). Microstructure design in mixed biopolymer composites. Food hydrocolloids. 15, 543-553.

Object Research Systems (ORS), Montreal, Canada (2018)

Ozturk, A.G., Ozturk, S.S., Palsson, B.O., Wheatley, T.A. & Dressman, J.B. (1990). Mechanism of release from pellets coated with an ethylcellulose-based film, *Journal of Controlled Release*. 14, 203–213.

Parmenter C.D.J., Fay M.W., Hartfieldm, C. & Eltaher, H.M. (2016). Making the Practically Impossible "Merely Difficult"—Cryogenic FIB Lift-Out for "Damage Free" Soft Matter Imaging. Microscopy Research and Technique. 79, 298-303.

Peyrega, C. & Jeulin, D. (2013). Estimation of tortuosity and reconstruction of geodesic paths in 3D. *Image Analysis & Stereology*, 32(1), 27–43.

Rawlings, J.M. & Lucas, M.L. (1985). Plastic pH Electrodes for the Measurement of Gastrointestinal pH. *Gut*. 26, 203-207.

Rhodes, C.T. & Porter, S.C. (1998). Coatings for Controlled-Release Drug Delivery Systems. *Drug Development and Industrial Pharmacy*. 24(12), 1139-1154.

Robinson, V.N.E. (1974). The elimination of charging artefacts in the scanning electron microscope. *Journal of Physics E: Scientific Instruments*. 8, 638-640.

Sakellariou, P. & Rowe, R.C. (1995). Interactions in Cellulose Derivative Films for Controlled Drug Delivery. *Progress in Polymer Science*. 20(5), 889-942.

Salzer, M., Spettl, A., Stenzel, O., Smått, J-H., Lindén, M., Manke, I. & Schmidt, V. (2012). A two-stage approach to the segmentation of FIB-SEM images of highly porous materials. *Materials Characterization*. 69, 115-126.

Schneider, C.A., Rasband, W.S. & Eliceiri, K.W. (2012). NIH Image to ImageJ: 25 years of image analysis. *Nature Methods*. 9(7), 671-675.

Schulenberg, H., Schwanitz, B., Krbanjevic, J., Linse, N., Scherer, G.G. & Wokaun, A. (2011). 3D imaging of catalyst support corrosion in polymer electrolyte fuel cells. *The Journal of Physical Chemistry*. 115, 14236–14243.

Schulz, H., Zeile, U., Stodolka, D. & Kaft, D. (2009). Advantages of a Local Charge Compensation System for FIB/SEM Applications on Insulating Materials. *Microscopy and Microanalysis*. 15(Suppl 2), 332.

Seligman, A.M., Wasserkrug, H.L. & Hanker, J.S. (1966). A new staining method (OTO) for enhancing contrast of lipid-containing membranes and droplets in osmium tetroxide-fixed tissue with osmiophilic thiocarbohydrazide (TCH). *The Journal of Cell Biology*. 30(2), 424-432.

Seliger, R.L., Ward, J.W., Wang, V. & Kubena, R.L. (1979). A high-inensity scanning ion probe with submicrometer spot size, *Applied Physics Letter*, 34 (5), 310-312.

Siepmann, F., Hoffmann, A., Leclercq, B., Carling, B. & Siepmann, J. (2007). How to Adjust Desired Drug Release Patterns from Ethylcellulose-Coated Dosage Forms, *Journal of Controlled Release,* 119, 182-189.

Siepmann, F., Siepmann, J., Walther, M., Macrae, R.J. & Bodmeier. (2008). Polymer Blends for Controlled Release Coatings, *Journal of Controlled Release*. 125, 1-15.

Siepmann, J., Siegel, R.A. & Rathbone, M.J. Editors: Fundamentals and Applications of Controlled Drug Delivery. Springer, New York, 2012.

Stenzel, O., Pecho, L., Holzer, M., Neumann. & V. Schmidt. (2016). Predicting effective conductivities based on geometric structure characteristics.*AIChE Journal*.62,1834-1843.

Stokse, D., *RMS - Royal Microscopical Society : Principles and Practice of Variable Pressure : Environmental Scanning Electron Microscopy (VP-ESEM)*. (2008). West Sussex, UK: John Wiley & Sons Ltd.

Subramaniam, S. (2005). Bridging the Imaging Gap: Visualizing Subcellular Architecture with Electron Tomography. *Current Opinion in Microbiology*. 8, 316-322.

Suzuki, E. (2002). High-resolution scanning electron microscopy of immunogold-labelled cells by the use of thin plasma coating of osmium. *Journal of Microscopy*. 208, 153-157.

Tanaka, K. & Mitsushima, A. (1984). A preparation method for observing intracellular structures by scanning electron microscopy. *Jounral of Microscopy*. 133, 213- 222.

Thiedmann, R., Hassfeld, H., Stenzel, O., Koster, L.J.A., Oosterhout, S.D. & Van Bavel, S.S. (2011). A multisacle approach to the representation of 3D images, with application to polymer solar cells. *Image Anal Stereol*. 30, 19-30.

Veroort, R.W., & Cattle, S.R. (2003). Linking hydraulic conductivity and tortuosity parameters to pore space geometry and pore-size distribution. *Journal of Hydrology*. 272, 36-49.

Villinger, C,. Gregorius, H,. Kranz, C,. Höhn, K,. Münzberg, C,. von Wichert, G,. Mizaikoff, B,. Wanner, G. & Walther, P. (2012). FIB/SEM tomography with TEM-like resolution for 3D imaging of high-pressure frozen cells. *Histochem Cell Biol*. 138, 549–556

Vogel, H.J. (1997). Morphological determination of pore connectivity as a function of pore size using serial sections. European Journal of Soil Science. 48, 365-377.

Walley, P.A., Wineberg, M. & Burden, M.ST J. (1971). The use of an electron beam evaporation source for electron microscope sample preparation. *Journal of Physics E: Scientific Instruments*. 4, 501-504.

Westermarcka, S., Juppob, A.M., Kervinena, L., and Yliruusib, J. (1999). Microcrystalline cellulose and its microstructure in pharmaceutical processing. *European Journal of Pharmaceutics and Biopharmaceutics*. 48, 199-206.

Wolff A,. Zhou Y,. Lin J,. Peng, Y.Y,. Ramshaw, J.A.M. & Xiao, Y. (2018). FIB/SEM Processing of Biological Samples. *Microscopy and Microanalysis*. 24(Suppl 1), 822.

Yang, S., Yin, X., Wang, C., Li, H., Xiao, T., Sun, L., Li, J., York, P., He, J., Zhang, J. (2014). Release Behaviour of Single Pellets and Internal Fine 3D Structural Features Co-define the In Vitro Drug Release Profile. *The AAPS Journal*. 16(4), 860-87.

Zils, S., Timpel, M., Arlt,T., Wolz, A., Manke, I. & Torh, C. (2010). 3D visualization of PEMFC electrode structures using FIB nanotomography. *Fuel Cells*. 10, 966-972.